ANL/ESD/11-39

Computational Mechanics Research and Support for Aerodynamics and Hydraulics at TFHRC, Year 1 Quarter 3 Progress Report

Energy Systems Division

About Argonne National Laboratory
Argonne is a U.S. Department of Energy laboratory managed by UChicago Argonne, LLC under contract DE-AC02-06CH11357. The Laboratory's main facility is outside Chicago, at 9700 South Cass Avenue, Argonne, Illinois 60439. For information about Argonne and its pioneering science and technology programs, see www.anl.gov.

Availability of This Report
This report is available, at no cost, at http://www.osti.gov/bridge. It is also available on paper to the U.S. Department of Energy and its contractors, for a processing fee, from:

U.S. Department of Energy
Office of Scientific and Technical Information
P.O. Box 62
Oak Ridge, TN 37831-0062
phone (865) 576-8401
fax (865) 576-5728
reports@adonis.osti.gov

ANL/ESD/11-39

Computational Mechanics Research and Support for Aerodynamics and Hydraulics at TFHRC, Year 1 Quarter 3 Progress Report

by
S.A. Lottes, R.F. Kulak, and C. Bojanowski
Transportation Research and Analysis Computing Center (TRACC)
Energy Systems Division, Argonne National Laboratory

August 2011

Argonne NATIONAL LABORATORY

Computational Mechanics Research and Support for Aerodynamics and Hydraulics at **TFHRC**

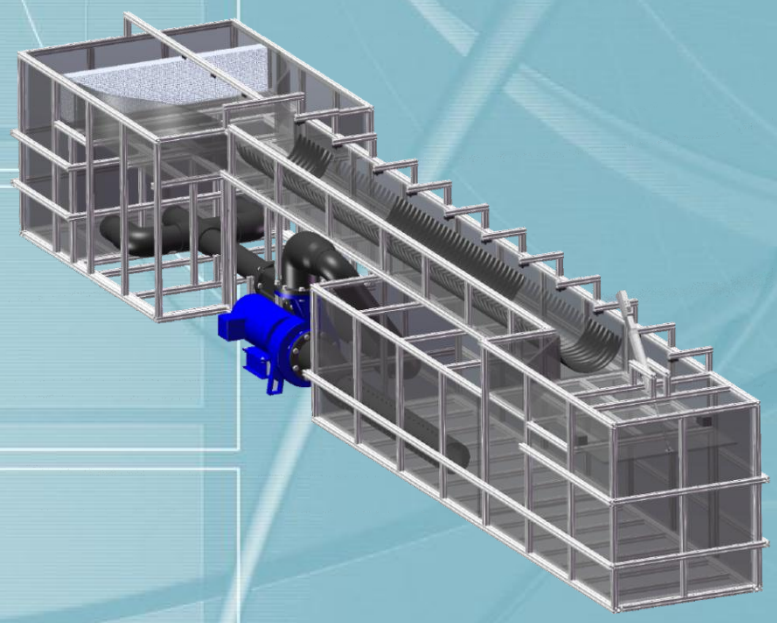

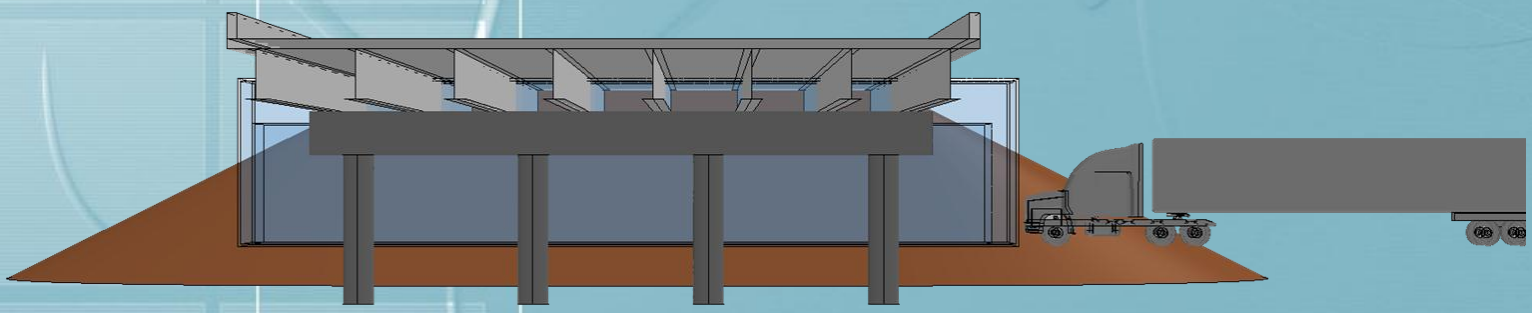

Quarterly Report

April through June 2011

Y1Q3

Computational Mechanics Research and Support for Aerodynamics and Hydraulics at TFHRC
Year 1 Quarter 3 Progress Report

Energy Systems Division (ES)
Argonne National Laboratory (ANL)

Principal Investigators:
Steven A. Lottes, Ph.D.

Ronald F Kulak, Ph.D., PE, FASME

Contributor:
Cezary Bojanowski, Ph.D.

Submitted to:
Federal Highway Administration

Kornel Kerenyi, Ph.D.
Turner-Fairbank Highway Research Center
Federal Highway Administration
6300 Georgetown Pike
McLean, VA 22101

Harold Bosch, Ph.D.
Turner-Fairbank Highway Research Center
Federal Highway Administration
6300 Georgetown Pike
McLean, VA 22101

August, 2011

Table of Contents

List of Figures

List of Tables

1. Introduction and Objectives

The computational fluid dynamics (CFD) and computational structural mechanics (CSM) focus areas at Argonne's Transportation Research and Analysis Computing Center (TRACC) initiated a project to support and compliment the experimental programs at the Turner-Fairbank Highway Research Center (TFHRC) with high performance computing based analysis capabilities in August 2010. The project was established with a new interagency agreement between the Department of Energy and the Department of Transportation to provide collaborative research, development, and benchmarking of advanced three-dimensional computational mechanics analysis methods to the aerodynamics and hydraulics laboratories at TFHRC for a period of five years, beginning in October 2010. The analysis methods employ well-benchmarked and supported commercial computational mechanics software. Computational mechanics encompasses the areas of Computational Fluid Dynamics (CFD), Computational Wind Engineering (CWE), Computational Structural Mechanics (CSM), and Computational Multiphysics Mechanics (CMM) applied in Fluid-Structure Interaction (FSI) problems.

The major areas of focus of the project are wind and water loads on bridges — superstructure, deck, cables, and substructure (including soil), primarily during storms and flood events — and the risks that these loads pose to structural failure. For flood events at bridges, another major focus of the work is assessment of the risk to bridges caused by scour of stream and riverbed material away from the foundations of a bridge. Other areas of current research include modeling of flow through culverts to assess them for fish passage, modeling of the salt spray transport into bridge girders to address suitability of using weathering steel in bridges, vehicle stability under high wind loading, and the use of electromagnetic shock absorbers to improve vehicle stability under high wind conditions.

This quarterly report documents technical progress on the project tasks for the period of April through June 2011.

1.1. Computational Fluid Dynamics Summary

The primary Computational Fluid Dynamics (CFD) activities during the quarter concentrated on the development of models and methods needed to complete the next steps in scour and culvert modeling. Work on identifying and fitting a sediment entrainment function to model transient pressure flow scour

experiments at TFHRC continued. A methodology to use transient CFD scour analysis itself to iteratively refine entrainment function parameters to match experimental results is proposed. Using the CFD software to tune empirical functions for the scour physics models is expected to produce more robust models for CFD analysis than those that are determined outside of the CFD framework. Work reported under the USDOT Y5Q3 report has been nearly completed on scour model enhancements needed to displace the bed in a direction normal to the bed instead of simply vertically, to account for the effect of bed slope on the scour rate, and to include a simple sand slide model to keep the bed slope less than or equal to the angle of repose of the sediment. These scour model enhancements will be incorporated into future scour modeling work.

Culvert analysis focused on determination of detailed velocity distributions to improve design procedures for culverts that need to allow for fish passage continued. A mesh refinement study for 22.86 cm (9 inch) flow depth cases was completed, and a 5 mm base mesh size with a 67% refinement in the corrugated region is recommended for CFD analysis of these cases in the TFHRC culvert test matrix. In another study, culvert modeling results were compared to experimental data obtained in two ways using Particle Image Velocimetry (PIV) and Acoustic Doppler Velocimetry (ADV). Differences between modeling results were within the range obtained with the two experimental methods and the results appear to be good enough to use for engineering analysis of culvert flow to improve the design procedures that allow for fish passage under low flow conditions.

1.2. Computational Multiphyics Mechanics Summary

Computational Multiphysics Mechanics Research for Turner-Fairbank Highway Research Center continued in the following four areas: (1) multiphysics simulation of salt spray transport; (2) simulation of a semi-trailer truck passing through a bridge underpass; (3) vehicle stability under high wind loadings; and (4) electromagnetic shock absorber for vehicle stability under high wind conditions. In Area 1, a literature search identified previous research performed at Lawrence Livermore National Laboratory from which estimates of the spatial distribution of the salt spray created by truck tires and the resulting density of the airborne salt water cloud behind the truck were extracted.

In Area 2, simulations were performed to study the motion of air as a semi-trailer truck approaches and passes through a bridge underpass and, in particular, to evaluate the transport of tire-generated salt spray onto the underside of bridges made from weathering steel. Marker particles at several levels above the roadbed were identified in the model and their motion as the truck approached and passed through the underpass was studied. In the direction of vehicle travel, only the particles near the top of the truck were found to reach the lower portions of the bridge support beams. This implies that should salt-laden air be at this level – which is implied from the Livermore research – then the salt spray could reach at least the flange level of the support beams. In the direction perpendicular to travel, it was found that as the truck approaches, the air from the roadway is pushed into the space between the beams, and as the truck exits, the air reverses direction and tends to move into the space vacated by the truck. TRACC staff and NIU staff (professor/student) continued working on two Wind Engineering projects.

The Area 3 work deals with the effects of wind loading on vehicles to evaluate rollover potential. A finite element model of a Ford F-800 truck was downloaded from the National Crash Analysis Center (NCAC). A wind pressure loading was applied to the one side of the truck, and studies on the resulting dynamic response have begun.

The Area 4 work is the development of an electromagnetic shock absorber control algorithm that can increase the stability of trucks driving in high wind conditions. New work done during the third quarter involved the analytical modeling of the electromagnetic shock absorber as well as its incorporation into the ¼ car Simulink model; the Simulink model utilizes an actual road profile as the disturbance for the system and the data is automatically exported into Microsoft Excel for post-processing. Also, finite element simulations of the Ford F800 truck model were performed to obtain mass, stiffness and damping properties.

2. Computational Fluid Dynamics for Hydraulic and Aerodynamic Research

The effort during the third quarter continued developing an approach to obtaining a good sediment entrainment rate function for pressure flow scour and continued development of methods for enhanced analysis of culvert flow for fish passage that account for the velocity distribution over a cross section.

2.1. Entrainment Functions for RANS Scour Models and Tests of Alternatives

Guo's [2] empirical formula for bed recession rate at the deepest point were used as the basis for obtaining a bed recession rate field function to morph the bed at any point on the bed as a function of the local shear stress. The formula was based on transient scouring experiments run at TFHRC and is given by:

$$Y = \left(1 - e^{-T/T_c}\right)^{0.25} \tag{2.1}$$

where Y is dimensionless time-dependent scour depth, defined as η/y_s in which η is the maximum depth of the scour hole at a given time and y_s is the final depth of the scour hole. T is dimensionless time, defined as tV_u/h_b where V_u is upstream velocity and h_b is height of the bottom of the bridge deck above the upstream (unscoured) bed. T_c = 1.56 X 10^5 is a characteristic dimensionless time parameter used to fit experimental data.

In terms of dimensional variables this becomes:

$$y = (1 - e^{-at})^{0.25} \tag{2.2}$$

where a = $V_u/(h_bT_c)$.

Equation (2.2) can be solved for t to give the laboratory time at which the scour hole reaches depth y:

$$t = -ln\left[1 - \left(\frac{y}{y_s}\right)^4\right] \tag{2.3}$$

Differentiating Equation (2.3) gives the bed recession rate at the point of maximum scour:

$$\frac{dy}{dt} = \frac{\frac{1}{4}y_s a e^{-at}}{[1 - e^{-at}]^{\frac{3}{4}}} \tag{2.4}$$

One problem with this fitted function is that the bed recession rate approaches infinity at time zero, which is physically unrealistic. The function fits the experimental data reasonably well after the first ½ hour, however, the actual bed recession rate at time zero in the TFHRC pressure flow scour experiments is a finite value that is a small fraction of a meter per second. Because over one third of the final depth of the scour hole may be reached in the first half hour, that time period is important in a CFD simulation that starts from time zero with a flat bed. Currently alternatives for dealing with a lack of data for the scour rate during the first half hour are being investigated.

Assuming that the entrainment rate is independent of time and a function of the local bed shear stress and bed slope, then Equations (2.3) and (2.4) can be used to fit an entrainment rate that is a function of shear stress at the point of maximum shear and that function can be applied anywhere on the bed. Three candidate functions are proposed. One by Xie [4] has the form:

$$E_b = ae^{b\tau_m} + ce^{d\tau_m} \tag{2.5}$$

in which τ_m denotes the maximum bed shear stress. E_b denotes the recession rate or sediment pickup rate. An initial fit yields the parameters: a = 2.933e-011, b = 4.034, c = -0.001206, d = -4.645. Initial testing of this function fit found that the scour away from the point of greatest depth was too slow and did not match the bed profiles at intermediate times.

The entrainment function by Van Rijn and a chemical kinetic rate law analogy proposed by Lottes [1] have been considered, and initial testing of these model functions for clear water pressure flow scour has begun. The Van Rijn function is a power law function of the form:

$$E_b = A_0\left(\frac{\tau}{\tau_c} - 1\right)^n \quad for\ \tau > \tau_c \tag{2.6}$$

$$E_b = 0 \quad for\ \tau < \tau_c \tag{2.7}$$

where E_b is the sediment pickup rate in units of mass per unit sediment bed area and per unit time, kg/(m^2 s). Initial tests using the constants given by Van Rijn yielded scour rates that were too fast and a pressure flow scour hole that was too deep, two or more times the experimental scour depth.

The rate law as proposed by Lottes [1] has the form:

$$E_b = A_0 \left(\frac{\tau}{\tau_c}\right)^n \exp\left(-\frac{A_1\,\tau_c}{\tau}\right) \tag{2.8}$$

where A_0, A_1, and n are fitting parameters. An initial fit of these parameters to the reduced experimental results by Guo yields

$$f(\tau) = (1.241e - 11)\tau^{12} exp(-0.564/\tau) \tag{2.9}$$

2.2. Initial Test of Mesh Morphing Applied to Transient Clear Water Pressure Flow Scour

An initial simulation using the bed recession rate given by Equation (2.9) was performed. The initial bed shear is shown in Figure 2.1. The bridge deck extends from 3.83 m to 4.09 m. The peak in shear is 9 cm from the trailing edge of the deck. The lower peak near x = 0.0 is due to a honeycomb at the inlet that straightens the flow, helps to ensure a uniform velocity across the flume, and strips off the boundary layer at the bed. The reforming boundary layer generates locally high bed shear extending to approximately x = 0.7 m. In that upstream zone the bed is fixed and cannot be eroded.

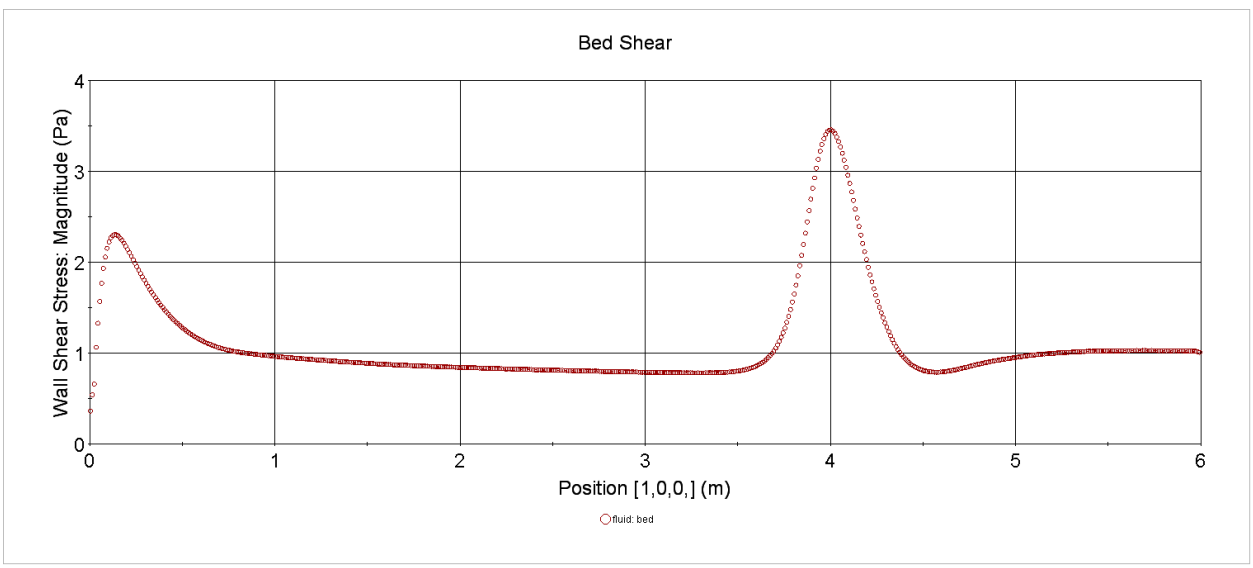

Figure 2.1: Initial bed shear profile along flume with flooded bridge deck at 3.83 m to 4.09 m

Figure 2.2 shows that the local peak in bed shear stress under the submerged bridge deck has dropped as flow area under the deck is increased through the erosion of bed material to a plateau that is near the critical value to initiate motion of stationary sediment particles on the bed.

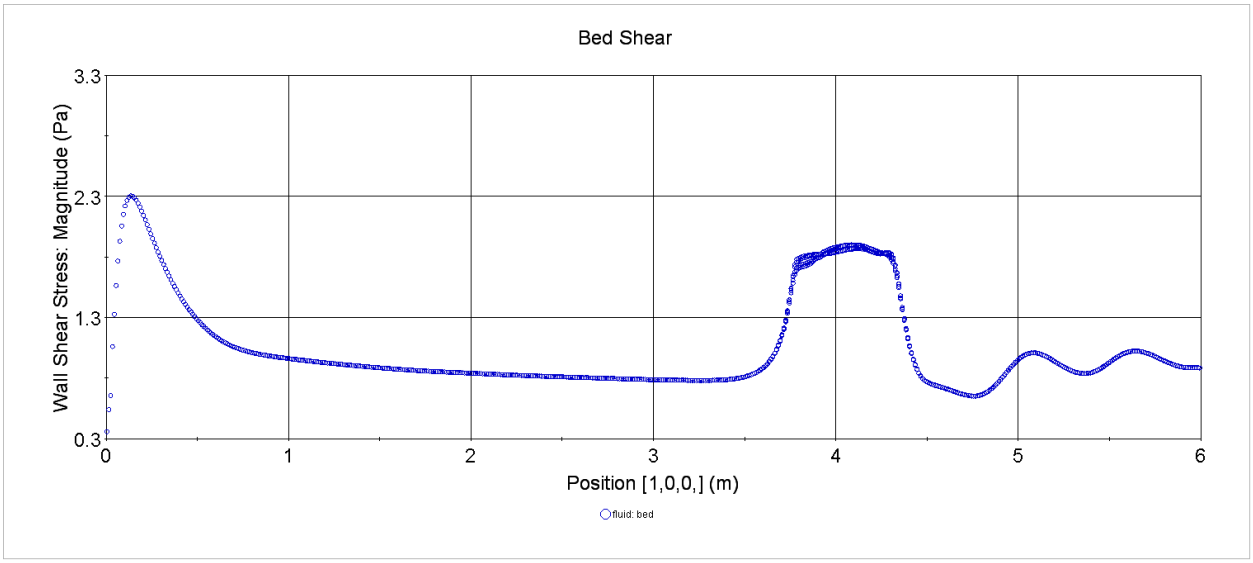

Figure 2.2: Bed shear after scour hole has fully formed

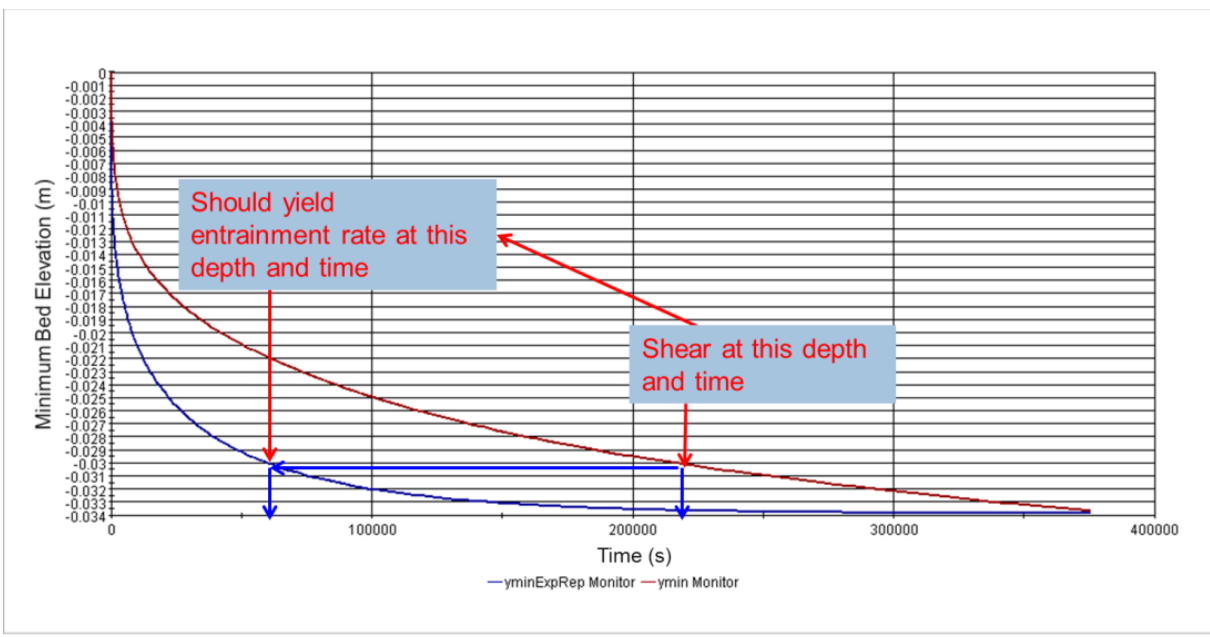

Figure 2.3: Development of scour hole depth for simulation (red) and experiment (blue)

A transient plot of scour hole depth from a simulation using Equation (2.9) for the bed recession rate is compared to the depth determined from Equation (2.2), which was derived by correlation with TFHRC experimental data by Guo [6]. The simulation was run out to 380,000 s (102 hour) where the scour depth from the simulation crosses the laboratory data fit. The experiment for the case was run for 151,200 s (42 hours). The rate function used in the simulation is too slow in the initial period, although that is not apparent in the figure due to the long time scale, and it is faster than the laboratory rate later, which allows it to eventually catch up. Figure 2.3 also shows a proposed procedure to iteratively

refine the rate function to improve the match to experimental results using the results of the CFD simulation. The CFD simulation yields the bed shear at the current scour depth at each time step. The laboratory time at which the simulated scour depth was reached can be computed from Equation (2.3), for times greater than 1800 s. Also for times greater than 1800 s, the bed recession rate at the depth from the simulation can be calculated from Equation (2.4). This procedure yields a new value for bed recession rate corresponding to the bed shear at the maximum depth for each time step. These new values can be used to improve the parameters for the entrainment rate function. As noted in Section 2.1, there are no experimental data for the first 1800 s, and the erosion rate at the deepest point as a function of time, Equation (2.4) has a physically unrealistic singular point at time equal to zero. In the absence of experimental data, some reasonable assumptions are needed to determine an erosion rate as a function of bed shear during the first 1800 s that will result in the simulation matching the experimental scour depth within the range of uncertainty at 1800 s. The procedure for achieving this goal is currently under development.

The streamwise velocity distribution in the vicinity of the flooded bridge deck at the initial unscoured state is shown in Figure 2.4. It clearly shows accelerated flow under the deck and a much higher velocity near the bed than in the upstream. Figure 2.5 shows the streamwise velocity distribution after the scour hole has fully formed. The accelerated flow under the deck is significantly reduced, and the near bed boundary layer is thicker, which yields a reduced shear stress peak under the bed and near zero erosion rate.

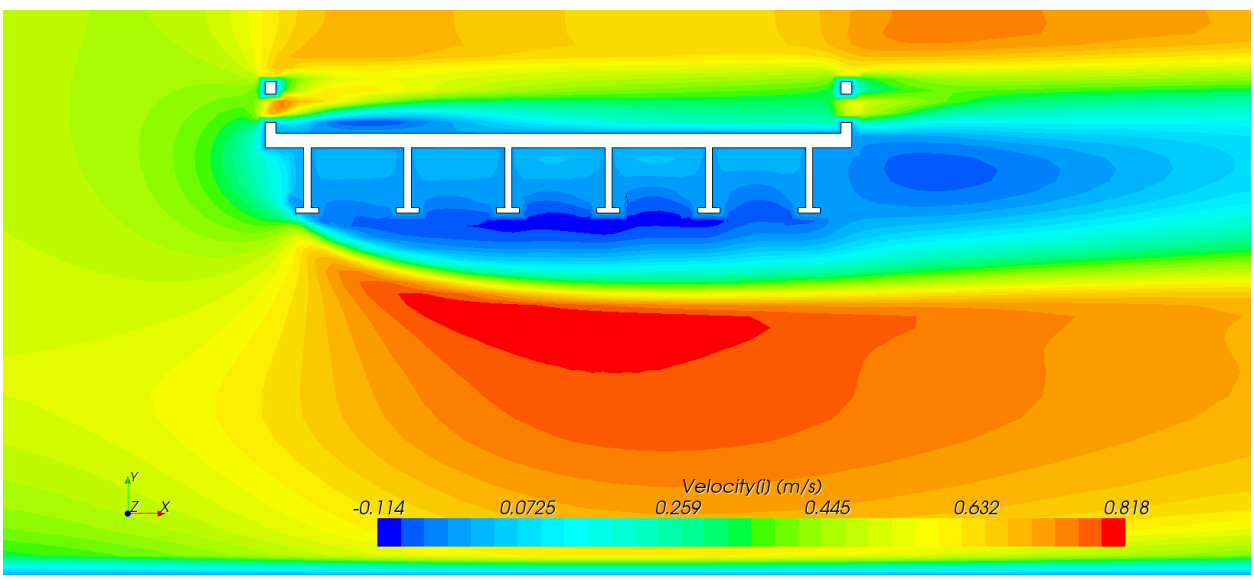

Figure 2.4: Initial streamwise velocity distribution around bridge deck

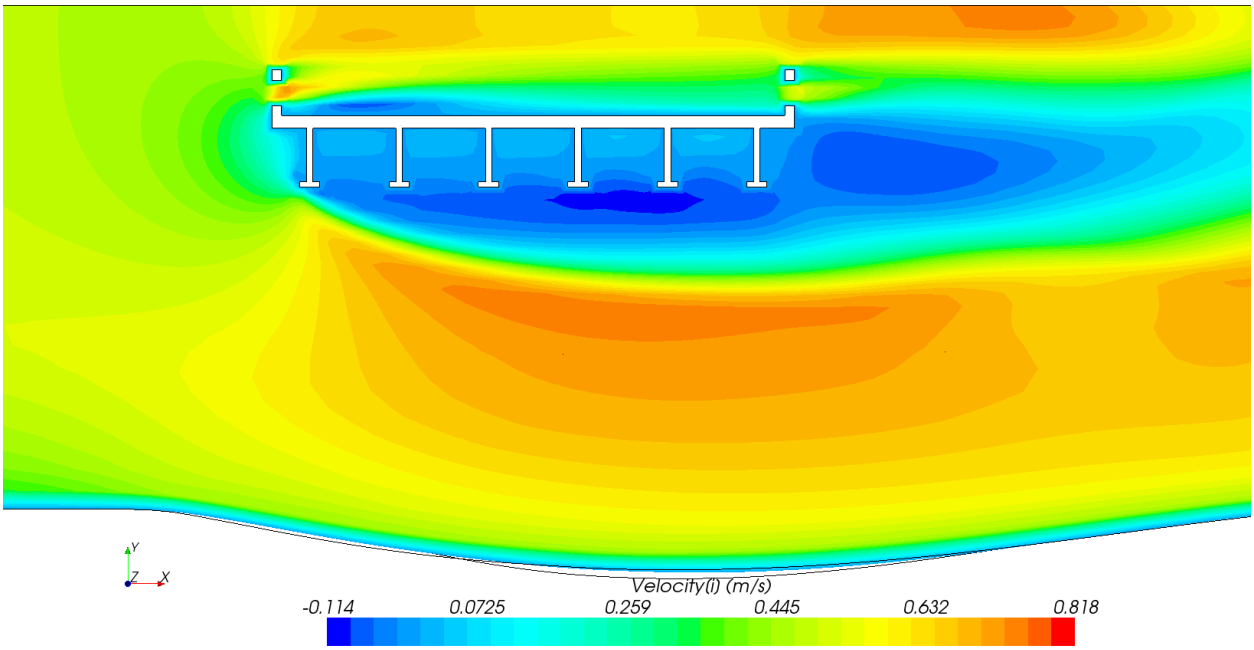

Figure 2.5: Final velocity distribution after scour around flooded bridge deck.

2.2.1. References

1. Lottes, S.A., *Hydraulics and Scour Modeling Notes*, unpublished, Argonne National Laboratory, 2011.
2. Guo, Junke, *Time-dependent scour of submerged bridge flows*, paper in preparation, Department of Civil Engineering University of Nebraska-Lincoln, 2011.
3. Guo, Junke, et.al., *Bridge Pressure Flow Scour at Clear Water Threshold Condition*, Trans. Tianjin Univ., 2009, 15;079-094.
4. Xie, Z., *Pressure Flow Scour Notes,* unpublished, University of Nebraska.

2.3. Computational Modeling and Analysis of Flow through Large Culverts for Fish Passage

Fish passage through culverts is an important component of road and stream crossing design. As water runoff volume increases, the flow often actively degrades waterways at culverts and may interrupt natural fish migration. Culverts are fixed structures that do not change with changing streams and may instead become barriers to fish movement. The most common physical characteristics that create barriers to fish passage include excessive water velocity, insufficient water depth, large outlet drop heights, turbulence within the culvert, and accumulation of sediment and debris. Major hydraulic criteria influencing fish passage are: flow rates during fish migration periods, fish species, roughness, and the length and slope of the culvert.

The objective of this work is to develop approaches to CFD modeling of culvert flows and to use the models to perform analysis to assess flow regions for fish passage under a variety of flow conditions. The flow conditions to be tested with CFD analysis are defined in the tables of a work plan from TFHRC [6]. The CFD models are being verified by comparing computational results with data from experiments conducted at TFHRC. A primary goal of CFD analysis of culverts for fish passage is to determine the local cross section velocities and flow distributions in corrugated culverts under varying flow conditions. In order to evaluate the ability of fish to traverse corrugated culverts, the local average velocity in vertical strips from the region adjacent to the culvert wall out to the centerline under low flow conditions will be determined.

A primary goal of the CFD analysis during this quarter has been to determine the local velocities and flow distributions through culverts for the fish passage with no gravel in the culvert. In order to more accurately evaluate the ability of fish to traverse culverts, it is desirable to look at the changes in the local average velocity of the flow adjacent to the culvert wall under low flow conditions. CFD runs using the cyclic boundary conditions to obtain the fully developed flow on a reduced 3D section of the culvert (symmetric quarter of the culvert section with corrugations from trough to another trough) have been conducted using CD-adapco's STAR-CCM+ software. Use of the cyclic boundary condition requires an assumption of a nearly flat water surface that can be modeled with a symmetric boundary condition that allows a free slip water velocity at that boundary. The cyclic boundary approach shortens the simulation time required to establish a fully developed flow with a known mass flow rate (with this approach several test cases can be completed per day). The periodic fully developed condition is achieved by creating a cyclic boundary condition, where all outlet variables are mapped back to the inlet interface, except for the pressure because there is a pressure drop corresponding to the energy losses in the culvert section. The pressure jump needed to balance the pressure drop for the specified mass flow is iteratively computed by the CFD solver. The runs were conducted with various mesh sizes, to take a closer look at how the velocity distribution and other flow parameters vary at different locations of the flow field by varying the base size of the mesh to obtain solutions that are effectively mesh independent. The mesh refinement study is also used to identify meshes that are computationally efficient while yielding good mesh independent results. An investigation of how the flow field varies for different cases such as reduced culvert section when considered from a trough to trough versus crest to crest. The computational model is based on the three-dimensional transient RANS k-epsilon turbulence model with wall function treatment.

The modeling work was done in collaboration with staff at TFHRC conducting physical experiments of culvert flows for the fish passage project in the Federal Highway Administration (FHWA). A preliminary comparison of the velocity distribution on the trough section between CFD model results and laboratory observation data was conducted. The 3D CFD model solves the Reynolds averaged Navier-Stokes (RANS) equations with k-epsilon turbulence model with wall function. The VOF method, which captures the free surface profile through use of the variable known as the volume of fluid was used in the multi-phase CFD model. The verification of the CFD model for engineering application using the laboratory observation data is a key step for the further work. A comparison of the multi-phase model and full scale flume single phase model was also done.

2.3.1. Model of Culvert Section with Fully Developed Flow Using Cyclic Boundary Conditions

In this study, a simulation model was developed using the commercial CFD software STAR-CCM+. A small section of the culvert barrel was modeled with cyclic boundaries at the inlet and outlet sections of the computational domain. A 36 inch diameter culvert with corrugation size 3 inches by 1 inch has been used for this study. The flow depth was 9 inches, a flow velocity was 0.71 feet/second, and zero bed elevation in the culvert (no gravel present).

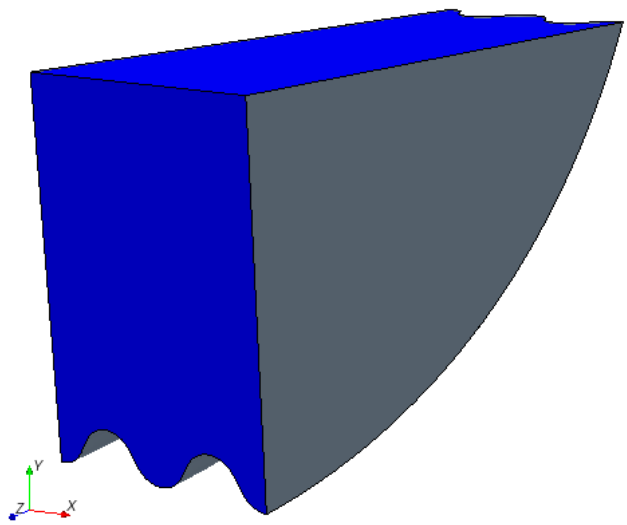

Figure 2.6: Reduced symmetric section of the barrel considered from a trough to trough

The boundary conditions used for the computational model in Figure 2.6 are listed in Table 2.1 below. All the CFD runs have been carried out with the same set of boundary conditions.

Table 2.1: Boundary conditions

Boundary	Name	Type
Face at minimum x value	Inlet	Cyclic boundary condition
Face at maximum x value	Outlet	Cyclic boundary condition
Water surface	Top	Symmetry plane
Centerline	Center	Symmetry plane
all other surfaces	Barrel	No-slip wall

2.3.2. Mesh Refinement Study

As detailed in the previous quarterly report, a CFD procedure is being developed to test the flow conditions that are defined in the tables of the work plan from TFHRC [6]. As a part of developing the procedure, mesh refinement studies are being conducted for each geometry configuration in the work plan. Sensitivity to mesh refinement will need to be checked for the larger culverts in the work plan when the geometry for those culverts are built. In the process of mesh refinement various base sizes have been chosen, along with the creation of a volumetric control (annulus ring) along the corrugated section. The refinement of the mesh is defined by specifying a reduction of mesh size for volume within an annulus intersecting the model as shown in Figure 2.7. The volumetric control body intersecting the corrugated section provides a means to refine the mesh in the corrugated region of interest. The refined mesh enables better resolution of the flow field with recirculation zones at the troughs between the corrugations. Meshing also includes a prism layer consisting of orthogonal prismatic cells running parallel to the wall boundaries, which constitutes a boundary mesh that is good for the application of wall functions to compute the shear stress at the wall boundaries.

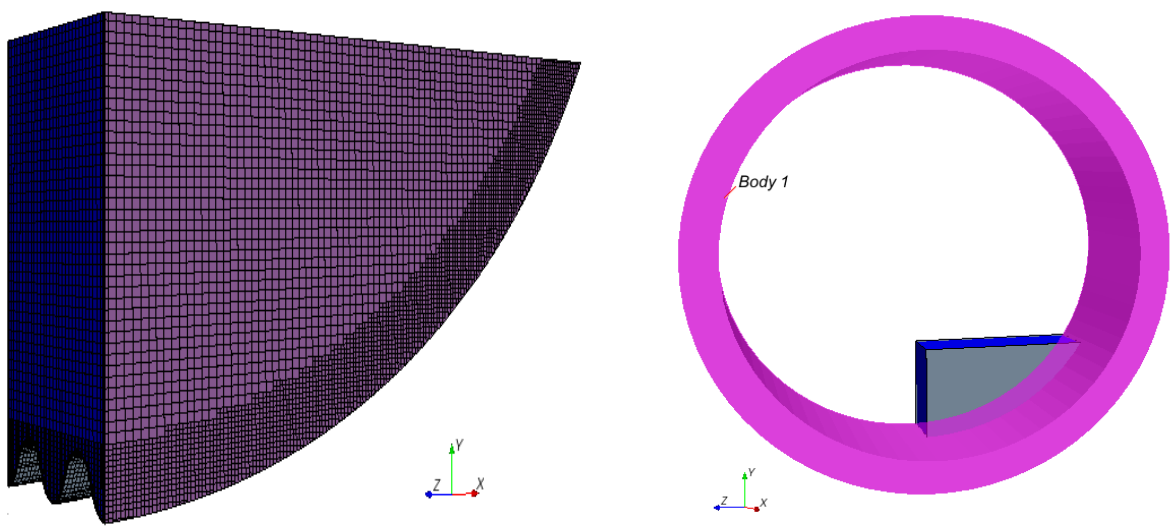

Figure 2.7: Refined mesh area with respect to the base created using a volumetric control

A volumetric control (annulus ring) was created intersecting the corrugated section to specially refine the mesh around this region with respect to the base as shown in Figure 2.7. Figure 2.8 does not show a coarser version of mesh 1 and mesh 4 because they look similar to mesh scenes 2 and 5 with larger cells. Sensitivity of the solution was tested with 6 variations of the mesh, including two base sizes and 4 combinations of refinement in the region with the corrugations where recirculation zones develop. The refinement is defined by specifying a reduction of mesh size for volume within a volumetric control as shown in Figure 2.7.

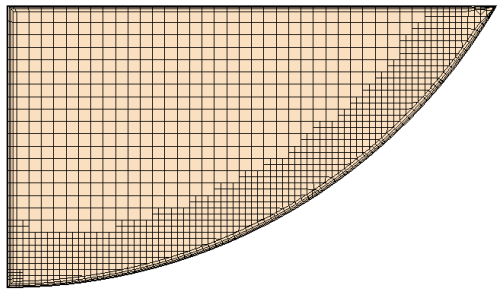

Mesh scene 2

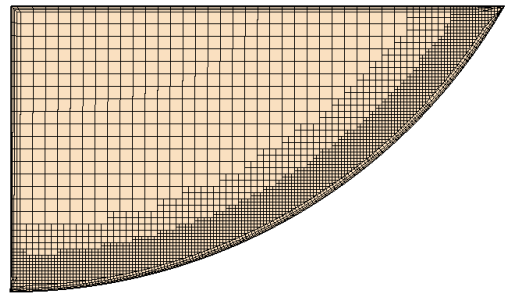

Mesh scene 3

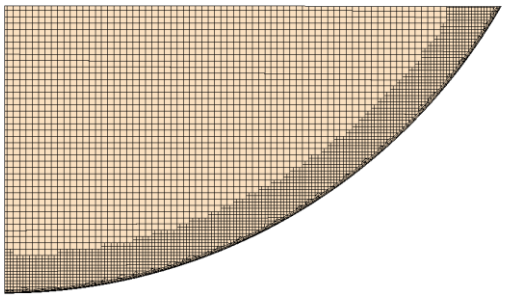

Mesh scene 5

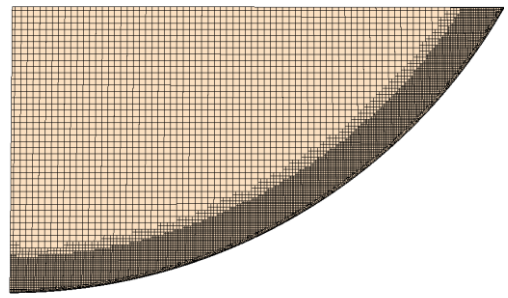

Mesh scene 6

Figure 2.8: Mesh scenes of the various cases used for mesh refinement studies

Table 2.2 below summarizes the details of the different cases considered in the mesh refinement study. For meshes 1 and 4, a uniform mesh size distribution with a mesh size of 10 mm and 5mm respectively has been chosen, other mesh types in Table 2.2 use volume controls for meshing to achieve a finer mesh with increased number of cells near the corrugated wall region to better resolve the recirculation zones in the region. A specified mass flow rate is given at the inlet and the outlet, which are the cyclic boundaries to obtain the cyclic fully developed flow condition. A mass flow rate of 13.85 kg/s was set for the cyclic boundary condition. The mass residuals decrease slightly for finer meshes, are good for all meshes, and don't nessarily indicate the accuracy of the computation.. The accuracy of the results obtained in terms of the velocity profiles at different sections in the flow field or the visualized scenes give a better picture of sensitivity to the mesh. The degree of convergence does not indicate the amount of discretion error. When the flow is not parallel to the cells in the mesh, there is some difference in the mass flow obtained by integrating over the cyclic boundary interface and a plane midway through the culvert section which gives some discretion error. The corrugations cause the flow streamlines to curve and not remain parallel to the mesh. Column 5 from Table 2.2 indicates the percent deviation of the mass flow across the boundary and mid plane. These values are all very good except for the coarsest mesh.

Table 2.2: Details of the various meshes used in the mesh refinement study

Case	Base size (m)	%Refinement in Corrugation Zone	Cells in Mesh	Mass Residual	% Deviation in Cross Section Mass Flow at a trough(mid-plane)	% Deviation in Cross Section Mass Flow at a crest
Mesh 1	0.010	None	18,910	2.32×10^{-7}	0.010	0.1
Mesh 2	0.01	50	58,803	2.44×10^{-7}	-0.005	0.002
Mesh 3	0.01	30	202,168	1.97×10^{-7}	0.008	0.018
Mesh 4	0.005	none	108,978	1.24×10^{-8}	0.029	-0.010
Mesh 5	0.005	66.6	249,174	3.35×10^{-8}	0.009	0.005
Mesh 6	0.005	40	887,369	2.8×10^{-8}	0.016	0.015

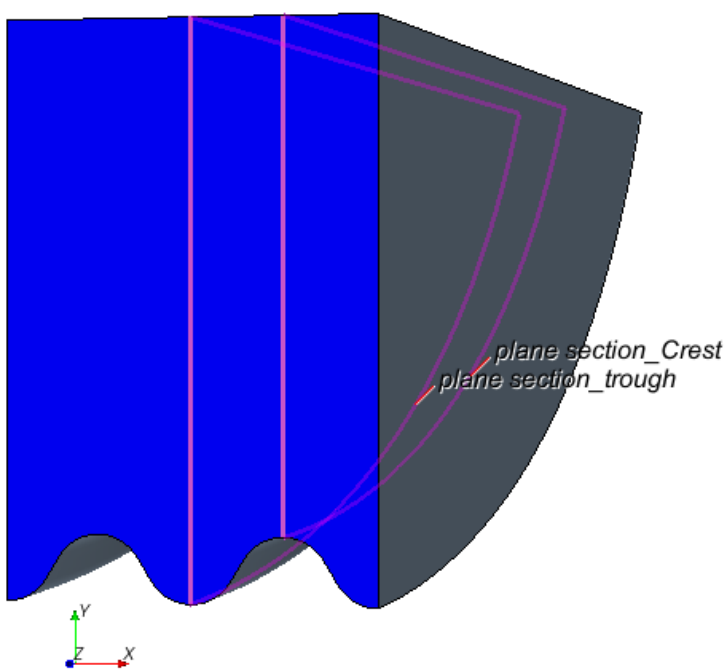

Figure 2.9: Sectional planes created at the trough and the crest to resolve flow parameters

Figure 2.9 shows the outline of plane sections defined in the geometry at a crest and a trough for analyzing the flow field velocity variation over culvert cross sections. The velocity distribution is analyzed by creating thin uniform strips, these uniform thin strips were created on a plane section (at the second trough in this particular case) using the post-processing features available in the STAR-CCM+ software.

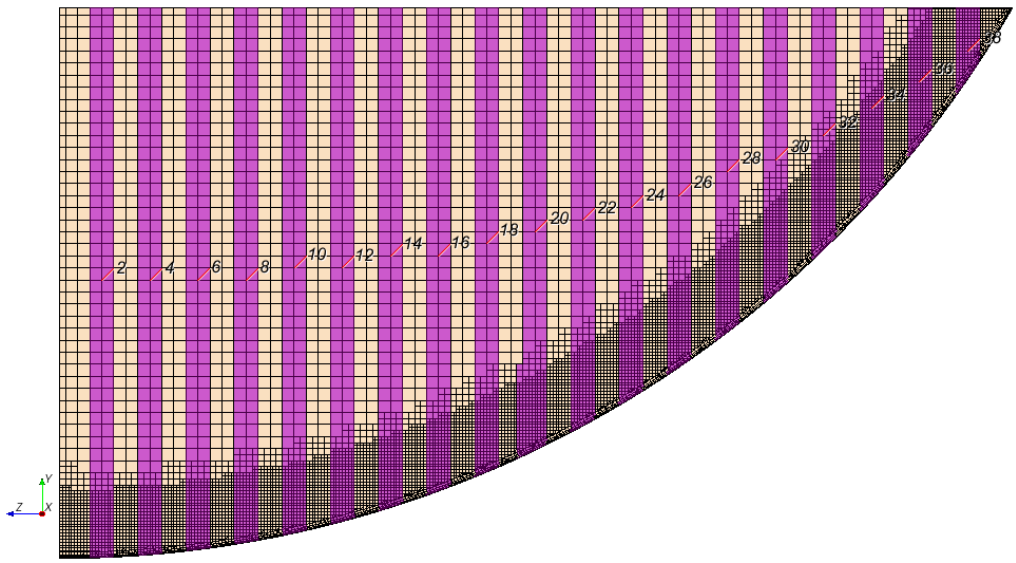

Figure 2.10: Uniform strips created using "Thresholds" feature available in STAR-CCM+

The uniform strips were created on the plane section at a trough in this case. Figure 2.10 shows only the even numbered strips created on the plane section at a trough. This procedure is carried out by creating multiple "Thresholds" of 1 cm width along the plane section. They are aligned with cell faces to avoid some interpolation error and obtain the best mean strip averaged velocity based on cell centroid values. After the thresholds are created, there is a "Report" feature available in STAR-CCM+ which calculates the surface averaged velocity of the uniform strip object.

2.3.3. Simulation Results and Discussion

2.3.3.1. Variation of the Surface-averaged Velocity over the Length of the Cross Section Studies:

In Figure 2.11 the trends of the curves (surface-averaged velocities on the plane section at the second trough) are plotted in MS-Excel along the length of the section. The x axis of the plot indicates the length of the plane section and the y-axis of the plot indicates the surface-averaged velocity. Each of these cases have the same base size of 10mm and refinement in the corrugated section for the two cases differ as mentioned in the plot are shown. For mesh 1, the curve indicating the trend of the surface-averaged velocity is irregular. Further, as the mesh is refined in the corrugated section the curves

indicating the surface averaged velocity of each of the uniform strips along the length of the plane section smooth out indicating that mesh refinement definitely affects the nature of the curve.

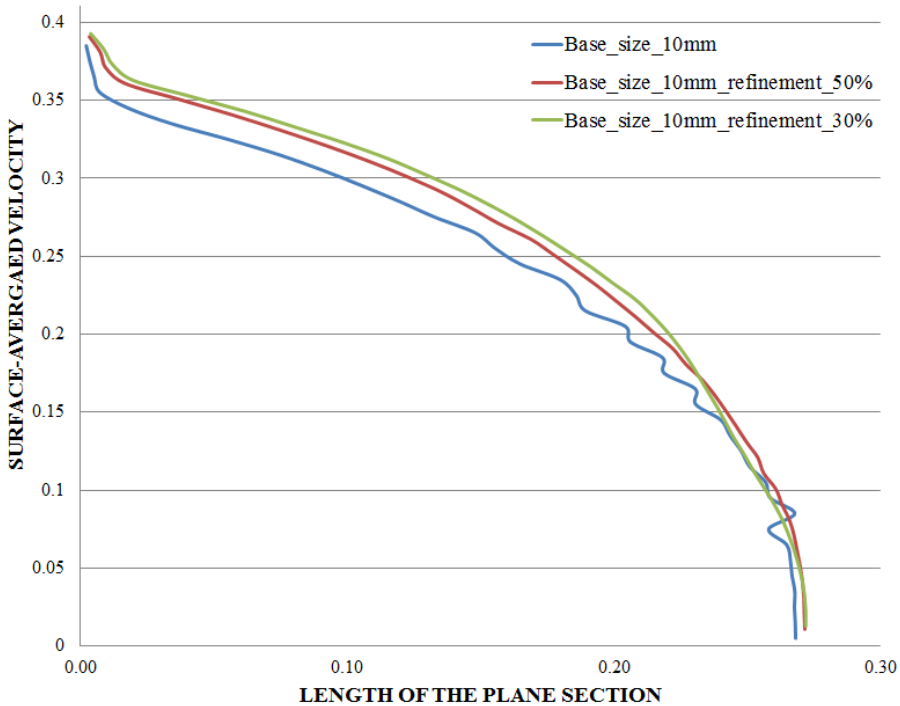

Figure 2.11: Surface averaged velocity vs. length of the plane section (created at a trough) plot for meshes 1-3

While looking at the curve for mesh 3, it is observed that the surface-averaged velocity along the uniform strips is not smoothened and the pattern of the curve is still indefinite with irregularities. This behavior of the curve for mesh 3 suggests that the flow resolution of the CFD model is grid independent beyond a particular value of mesh refinement. Thus the procedure of creating "Thresholds" and generating reports to output the surface-averaged velocity for various mesh cases helps in identifying the optimum value of the base size of the mesh and also the extent to which the mesh could be refined in the corrugated section.

The same procedure of creating the strips using thresholds and generating the reports is followed for meshes 4-6, the only difference here being the base size of the mesh is 5 mm. A volumetric control is used in the corrugated section for mesh 5 and 6 where the mesh is further refined in comparison with the base size of the mesh. The curve for mesh 4 is observed to be smooth. When the mesh 5 is further refined, the surface-averaged velocity plotted along the length of the cross section is slightly different

from that of mesh 4 but close, and either would be adequate for engineering purposes. When the corrugated section is further refined with respect to the base in case of mesh 6, the path of the curve is initially as expected but contains an irregular ripple. The cause of this effect is currently unknown.

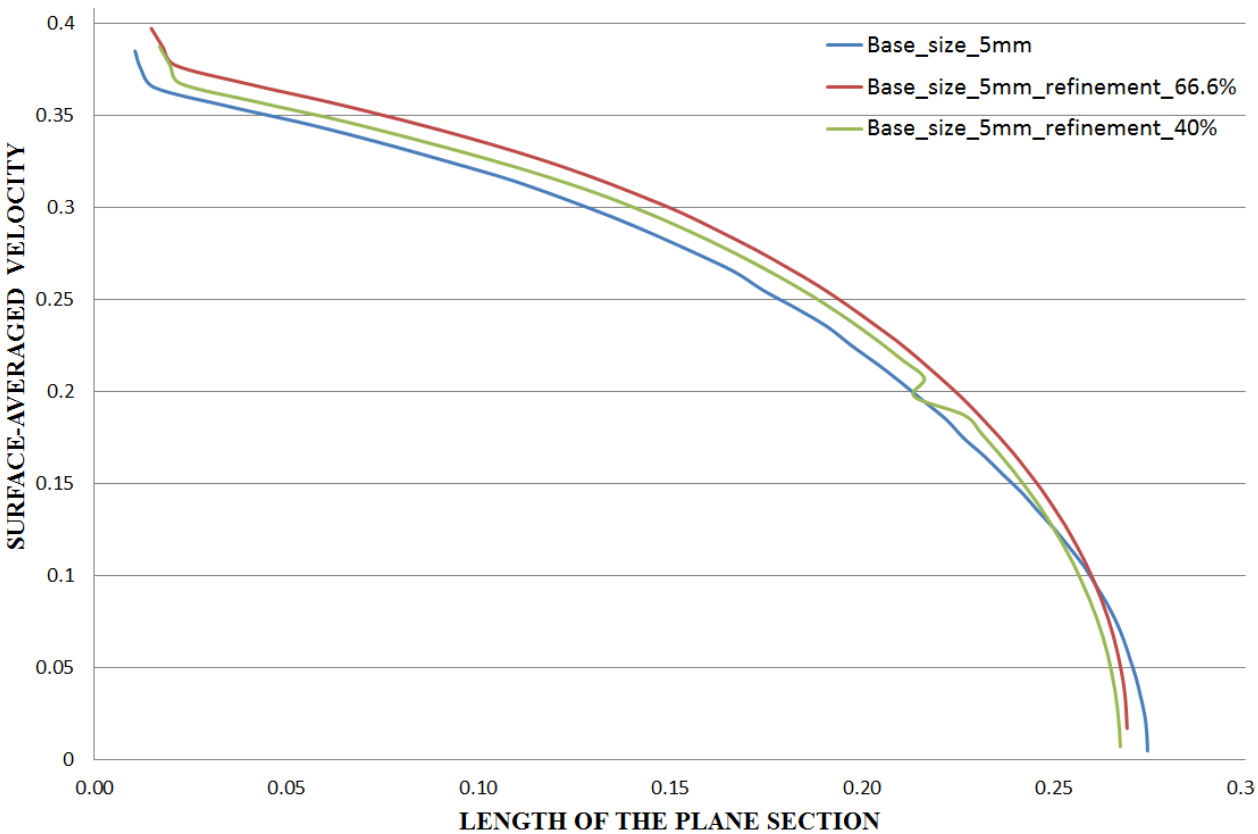

Figure 2.12: Surface averaged velocity vs. length of the plane section (created at a trough) plot for meshes 4-6

2.3.3.2. Velocity Profile Variation with Mesh Refinement

Line probes have been created along the flow section in the STAR-CCM+ software. In this particular case line probes have been created at a trough and a crest which are the regions of major interest. Each of the line probes created has 30 points on the line. The value of the Velocity magnitude of the flow is extracted at that particular point. Velocity profiles have been plotted using the line probes at a trough and a crest along the reduced barrel section. By taking a close look at the velocity profiles, it is possible to better analyze the nature of the flow.

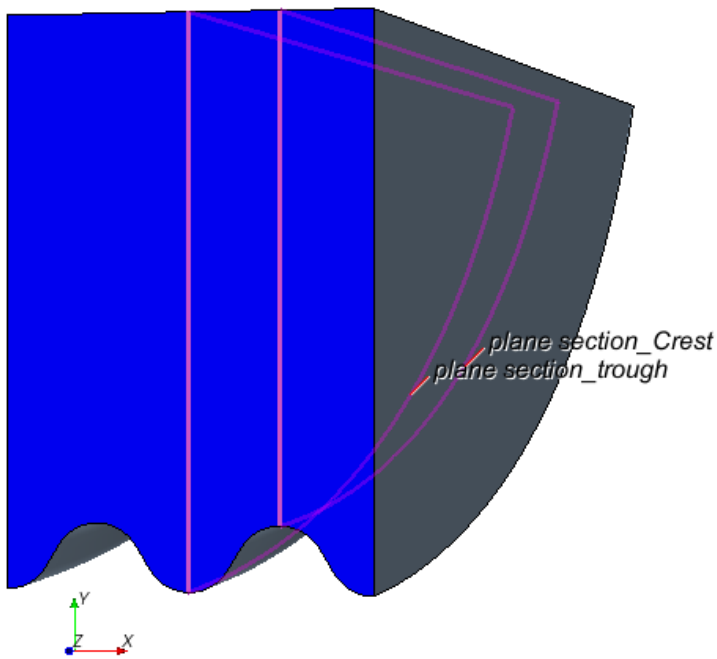

Figure 2.13: Line probes created at a trough and a crest along the flow field in the reduced barrel

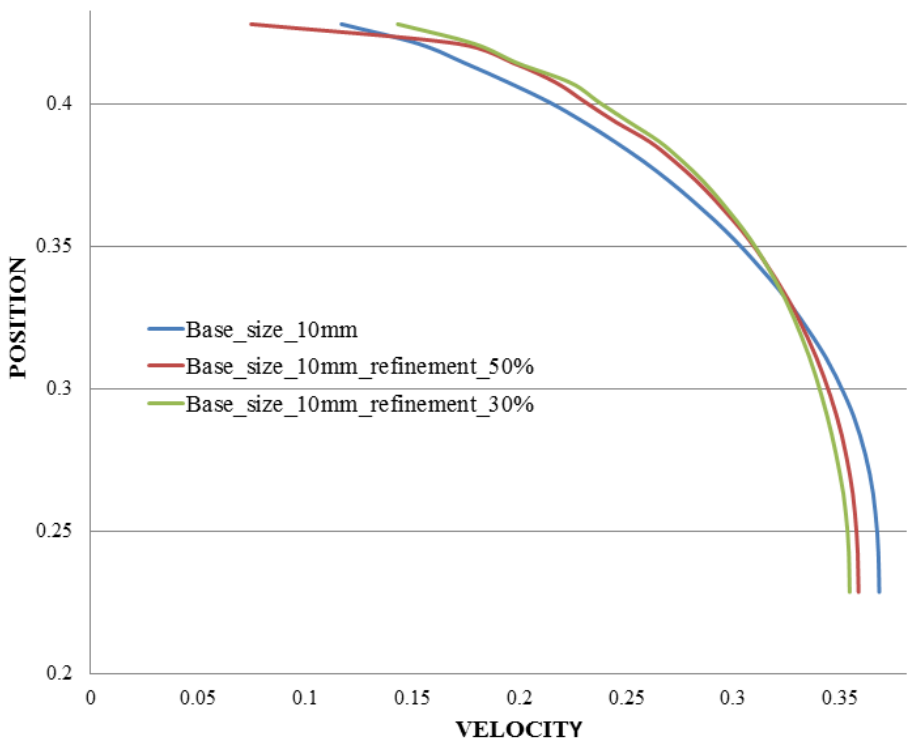

Figure 2.14: Velocity profiles of the different mesh cases with base size as 10mm plotted at a crest

In Figure 2.14, the x-axis of the plot represents velocity and the y-axis represents the position of the line probe at a trough in the vertical direction. The minimum unit on the y-axis is 0.2 m and the maximum unit is 0.4572 m. The y coordinate of the boundary representing the water surface (namely the top of the reduced culvert section in the CFD study) is at 0.2286 m and the y coordinate of the boundary representing the bottom of the culvert at the wall in 0.4572 m. The same CAD model has been used for all the CFD simulations with the co-ordinates of the reduced symmetric barrel section considered from a trough to a trough as mentioned above. The top surface of the culvert is simulated as a symmetry plane as mentioned previously which represents an imaginary plane of symmetry in the simulation. It implicates an infinitely spread region modeled as if in its entirety. The bottom of the culvert is simulated as a wall with a no slip condition. When velocity is plotted against position, the velocity at the wall is zero, the first point plotted is the velocity in the cell next to the wall and increases with distance from the wall. In Figure 2.14, the velocity profiles change as the base size of the mesh is varied. All of these cases show some mesh dependence but may be adequate for engineering analysis of fish passage. However, because cases using the relatively small geometry of a barrel section with periodic boundary conditions complete in a short time further mesh refinement was investigated.

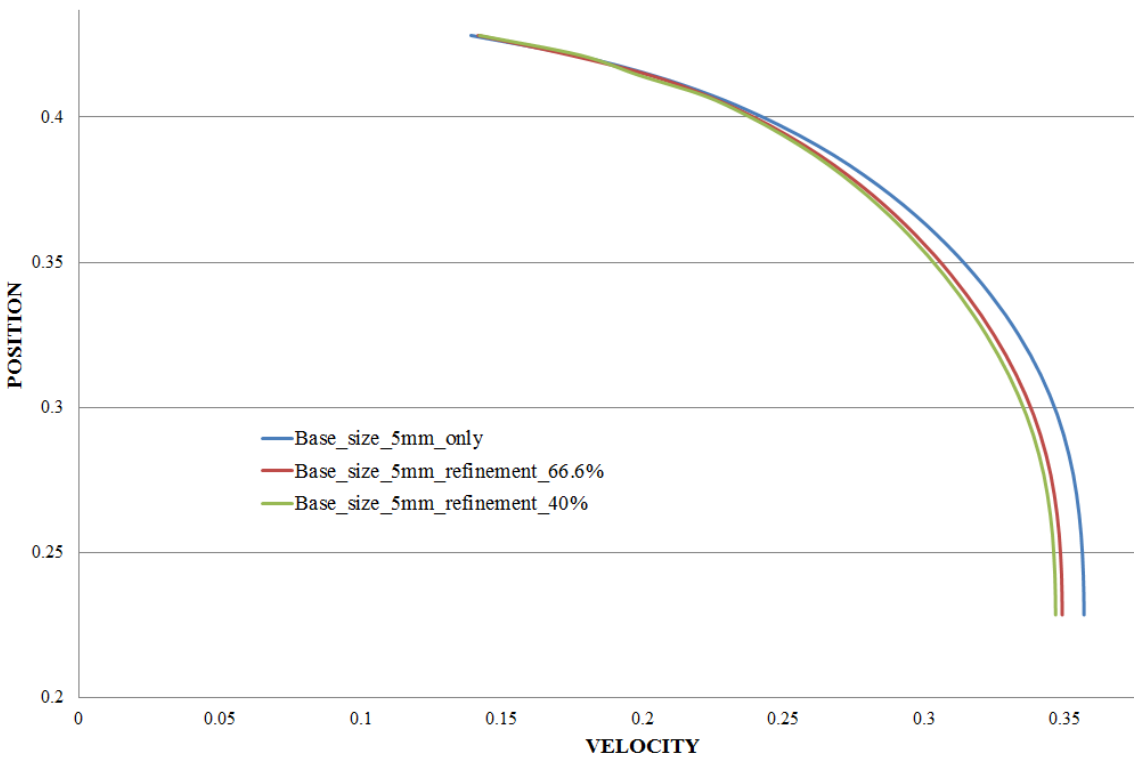

Figure 2.15: Velocity profiles of the different mesh cases with base size 5mm plotted at a crest

In Figure 2.15 the velocity and the position corresponding to the line probe (at a crest) are represented on the x and y axis of the plot. With a mesh base size of 5mm, the velocity profiles are very regular. For the mesh case where the base size is 5mm and no refinement in the corrugated section, the maximum velocity is a little higher than cases with further refinement in the corrugations. For mesh cases 5 and 6 where the mesh is further refined along the corrugated section in the order of 80% and 66% respectively there is not much difference in the nature of the velocity profiles although there is large difference in the number of computational cells. Mesh case 5 consists of 249,174 cells and mesh case 6 consists of 887,369 cells. Mesh 5 is reasonably mesh independent upon further refinement and consumes a reasonably small amount of computational resources.

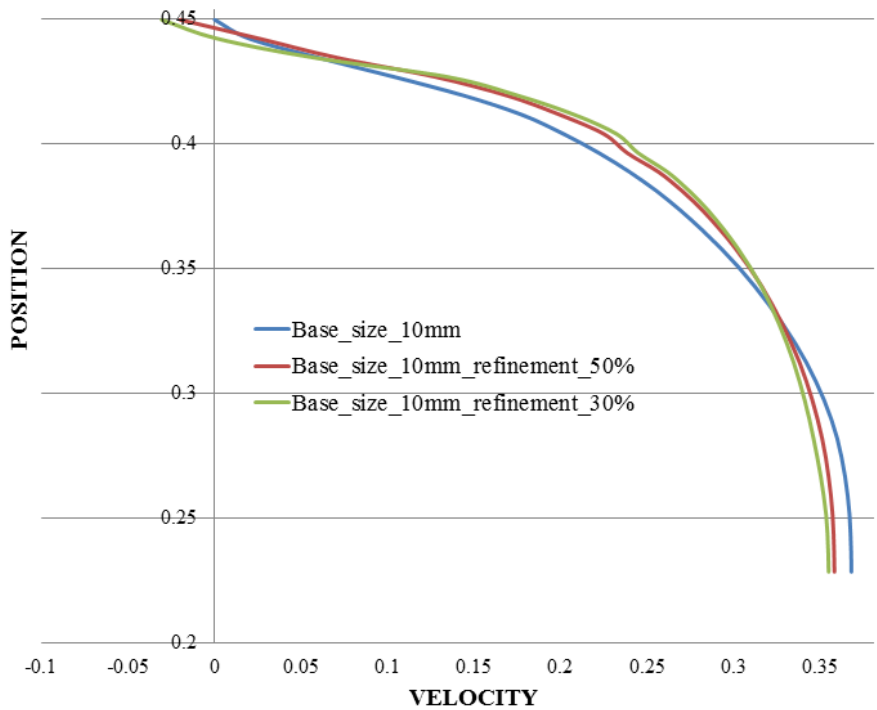

Figure 2.16: Velocity profiles of the different mesh cases with base size 10mm plotted at a trough

In Figure 2.16 the velocity profiles of the various mesh cases with base size 10 mm are plotted at a trough using line probes. The x-axis has a negative scale due to reverse flow in the recirculation zones in a trough. One of the benefits of flow simulation is that it provides detailed information about recirculation. Recirculation regions in the flow field are of particular interest since their presence can have a significant impact on the nature of the flow. As seen in Figure 2.16, there is a difference in the velocity profiles for the various mesh cases. The mesh case 4 has not been able to capture the effect of flow recirculation, but as the mesh is further refined along the corrugated section the recirculation of the flow can be resolved.

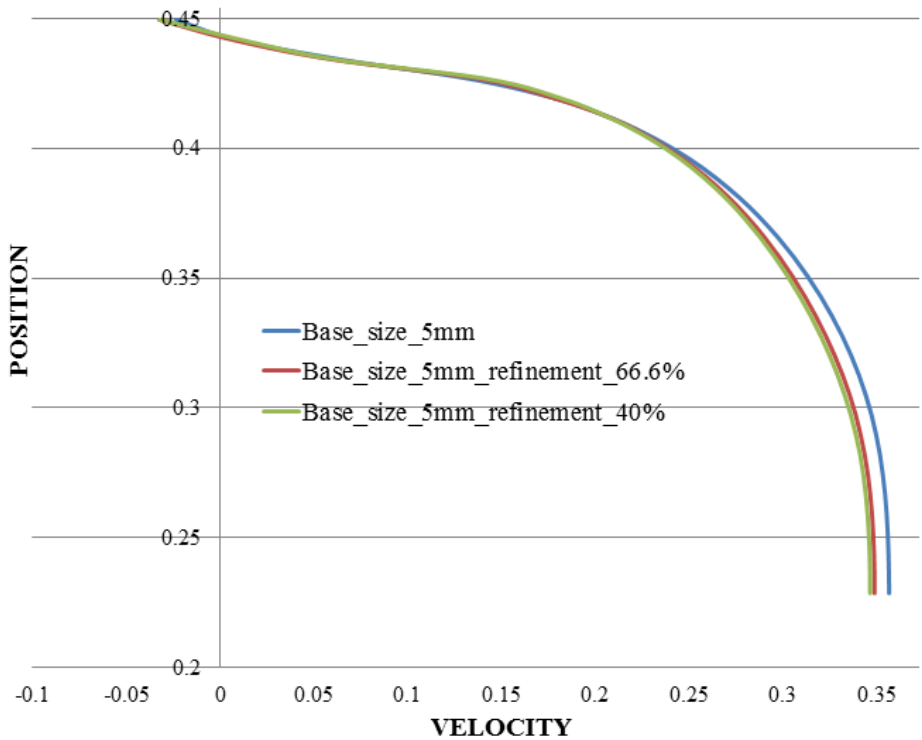

Figure 2.17: Velocity profiles of the different mesh cases with base size 5 mm plotted using at a trough

In Figure 2.17, velocity profiles for the different mesh cases with base size 5 mm at a trough are plotted. The 5 mm base size with a 66.6% refinement in the trough appears to be the coarsest mesh that is mesh independent.

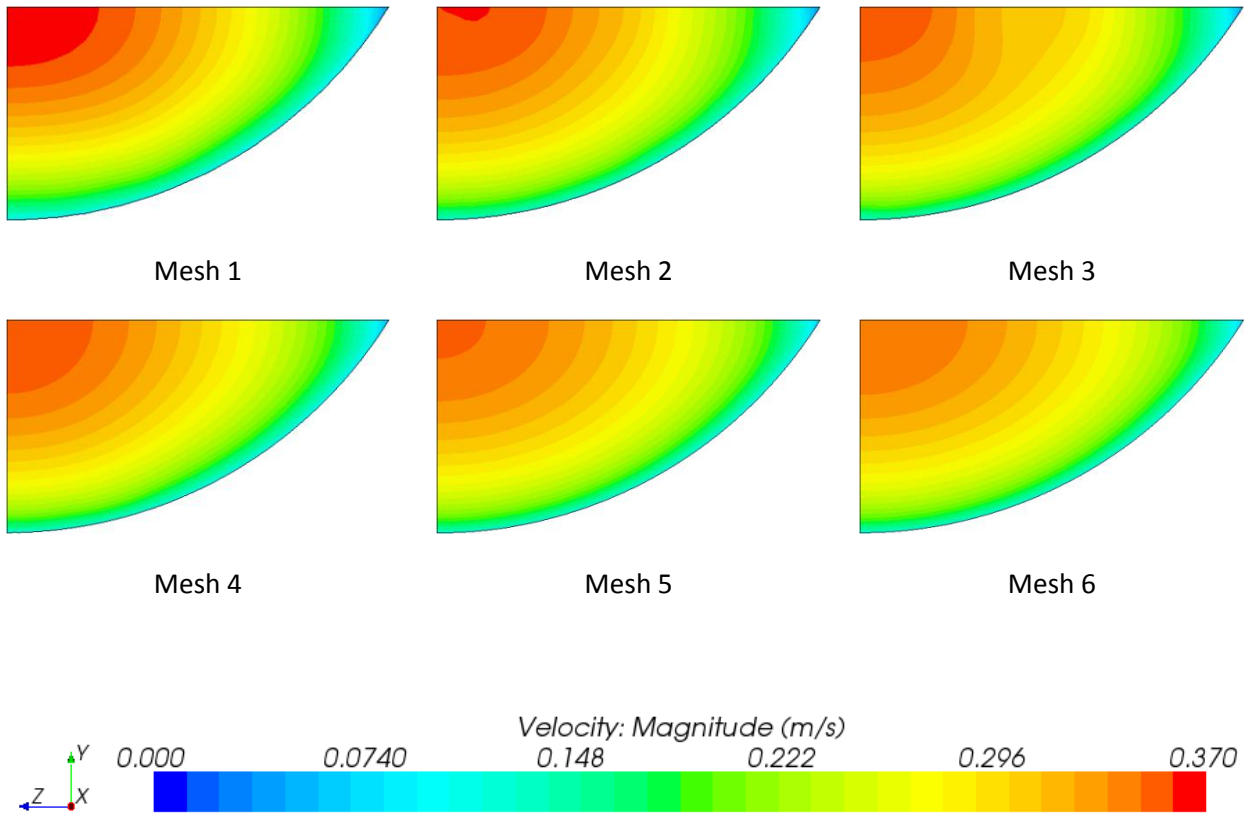

Figure 2.18: Velocity plots of the various mesh cases in the mesh refinement study

The above Figure 2.18 contains the velocity distribution scenes of all the various mesh cases used for the mesh refinement study plotted at a crest.

Mesh Refinement Conclusions: The mesh refinement studies have been conducted for various base sizes of the mesh for the symmetric reduced barrel section (considered from a trough to a trough) to choose the optimum base size of the mesh and also the refinement that needs to be done in the corrugated section. By analyzing the variation of the surface averaged velocity with respect to the length of the plane section at a trough and the velocity profiles plotted using line probes at a trough and a crest the optimum mesh can be selected. With all the CFD analysis done on a 36 inch diameter of the culvert with corrugation size 3 inches by 1, for a flow depth of 9 inches and a flow velocity of 0.71 feet/second for zero bed elevation of the culvert, in terms of mesh refinement studies, mesh 5 with a 5 mm base size and 67% refinement in the corrugation region, which yields a mesh with about 250,000 cells gives mesh independent simulation results with adequately fast run times.

2.3.4. Three Dimensional Model of Culvert Flume with Comparison to Experimental Results

The preliminary objective of this study was to develop a computational fluid dynamics (CFD) model to characterize the three-dimentional (3-D) two-phase (air and water) laboratory model associated with three different water depths, two different velocities and three bed elevations. The suitability of the CFD model for fish passage engineering analysis is assessed by comparison with experimental data obtained from TFHRC. In phase 1 of the study, a three-dimentional multi-phase CAD model, as shown in Figure 2.19, was created in Pro-ENGINEER. The CAD model consists of three parts along the flow direction (z axis): the intake, the barrel and the diffuser. Since the two-phase VOF model (water and air) is used for numerical simulation, initially an air layer was included on top of the water domain in the vertical direction (x axis). The culvert model considered in phase 1 of study is the symmetrical half of the culvert pipe having annular corrugations without bed elevation as shown in Figure 2.19.

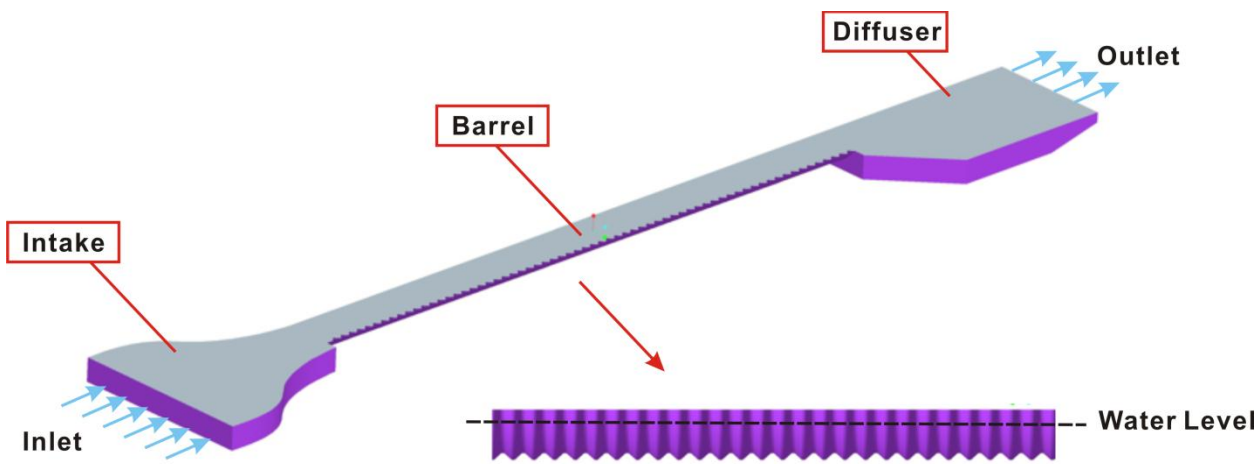

Figure 2.19: Three-dimensional CAD model for multi-phase simulations

The experiments in this study were conducted at the FHWA J.Sterling Jones Hydraulics Laboratory, located at the TFHRC. The experiments were conducted in a circulating flume. Figure 2.20 provides the details of the experimental flume dimensions in front and overlook views. The corrugations used are 3 inch by 1 inch annular. Three typical cross sections were monitored in the tests, which were located at the inlet of the barrel (section 1), the middle of the barrel (section 2) and the end of the barrel (section 3), respectively.

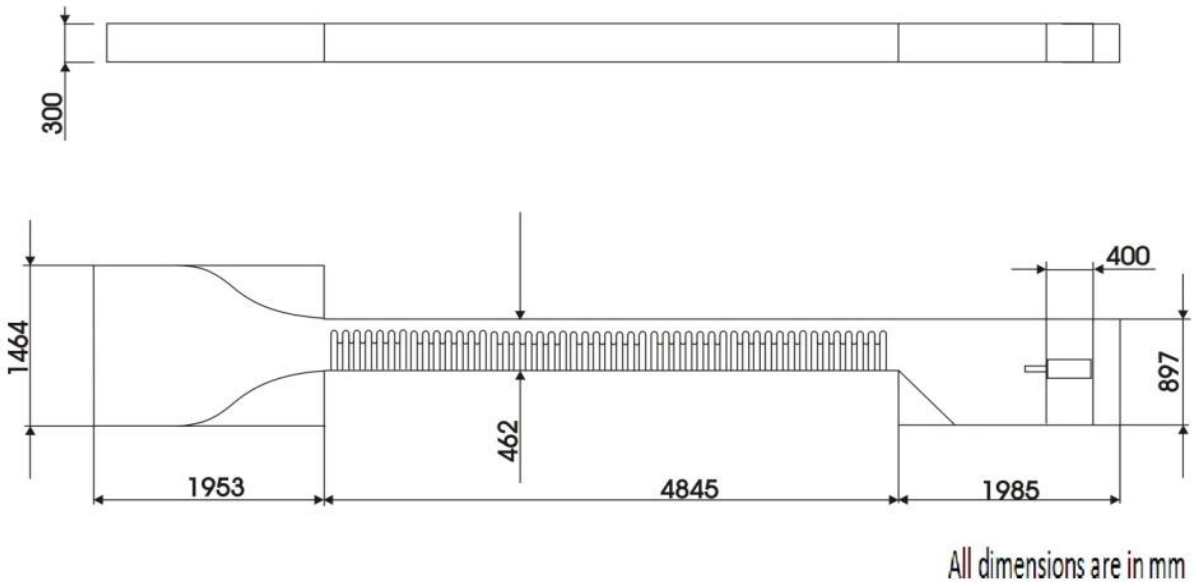

Figure 2.20: Dimensional details of the flume (front and top views)

The primary purpose of running CFD tests on a three dimensional model of the full TFHRC culvert test flume is to verify that the much smaller domain of a barrel section with cyclic boundary conditions can be used for parametric runs to determine zones for fish passage. A significant difference in the two models is that the small section using a cyclic boundary condition must be run as a single phase flow with a symmetric, free slip boundary condition at the water surface. This requires that the flow be deep enough for the corrugations to have negligible effect on the surface. Truncated CFD models with cyclic boundaries can be utilized as a time-effective tool in completing the large test matrix of the project.

2.3.5. Flow Conditions

All the test scenarios in the study involve three different water depths, two velocities, and three bed elevations. Additional design parameters include tilting angle of the flume, open angle of the flap gate, roughness parameters etc.. The flow conditions for the completed multi-phase CFD model tests are listed in Table 2.3.

Table 2.3: Flow conditions

Water Depth	3 inch	6 inch	9 inch
Bed elevation	0	0	0
Air depth(inch)	2.5	3	2.5
Mean velocity (m/s)	0.2164	0.2164	0.2164
Tilting angle of the flume (degree)	1	0.125	0.07
Tilting angle of the flap gate with respect to the horizontal (degree)	12.5	18	28

2.3.6. Results Using VOF Multiphase Model

Velocity distributions are plotted over a plane cut through a culvert barrel trough that is located in the middle of the culvert. For each water depth, the velocity distribution across the whole multi-phase cross-section is given on the left, and the plot on the right covers only the lower zone containing water. Also, the 0.5 VOF curves are plotted on top of the velocity contours, which indicate the corresponding water surface. The results for 3 inch, 6 inch, and 9 inch water depth are illustrated in Figure 2.21, Figure 2.22, and Figure 2.23 respectively.

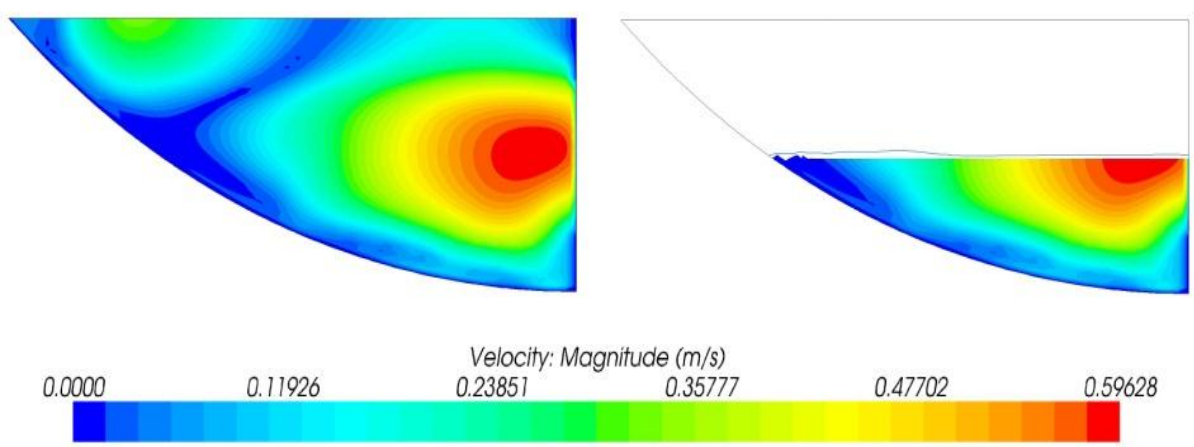

Figure 2.21: Velocity distribution across trough section of the multi-phase model for 3 inch water depth

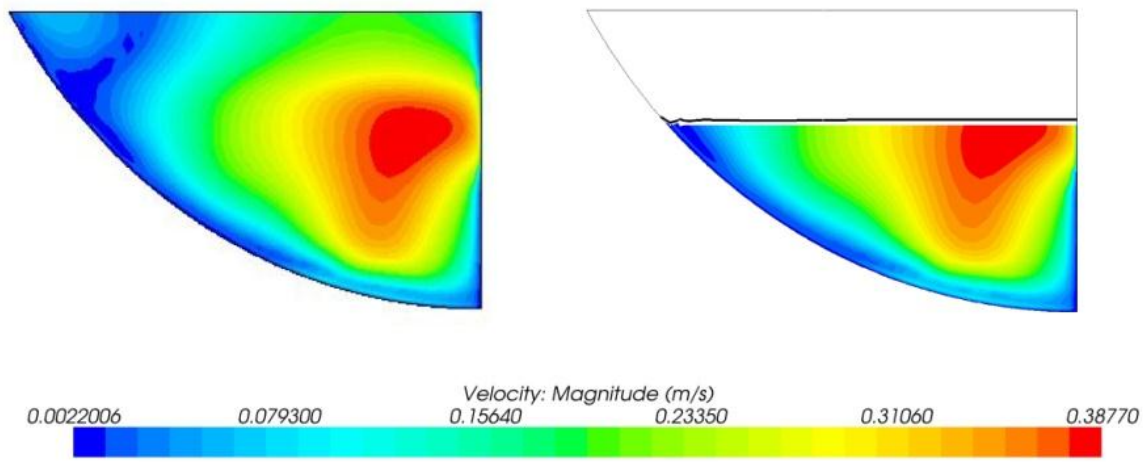

Figure 2.22: Velocity distribution across trough section of the multi-phase model for 6 inch water depth

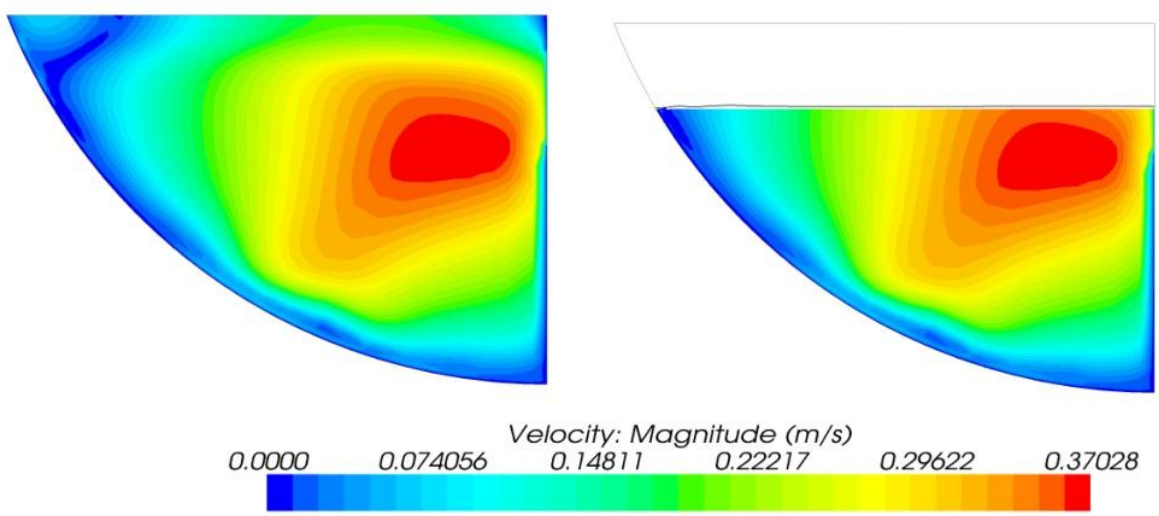

Figure 2.23: Velocity distribution across trough section of the multi-phase model for 9 inch water depth

2.3.7. Comparison with the Single Phase Model

In the multi-phase CFD model for the full-scale flume, if the longitudinal VOF changes indicate that the water level is nearly flat along the culvert, it is possible to set up a single phase model to simulate the flow. Figure 2.24 illustrates the comparison of the velocity distribution between the multi-phase model and full scale single phase model for 6 inch water depth. Note that the maximum velocity occurred in the single phase case is 0.42 m/s, which is larger than 0.38m/s in the multi-phase case.

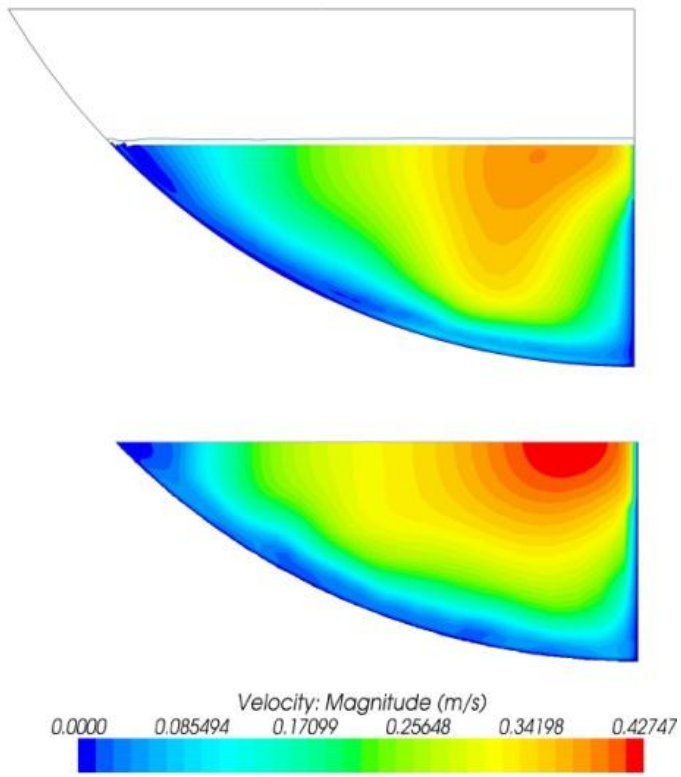

Figure 2.24: Multi-phase model vs. full flume single phase model illustrating velocity distribution across trough section for 6 inch water depth

2.3.8. Comparison with Laboratory Data

Particle Image Velocimetry (PIV) and Acoustic Doppler Velocimetry (ADV) are two methods used to capture the velocity data from laboratory experiments. Acoustic Doppler Velocimeters are capable of reporting accurate values of water velocity in three directions even in low flow conditions. The main objective of the PIV tests is to obtain a 3-dimensional high-resolution velocity distribution, which is convenient for visual comparisons with CFD results.

Comparisions of the CFD data with laboratory data for 6 inch and 9 inch water depths have been done. The agreement levels between multi-phase model results and experimental results for 6 inch water depth are depicted in Figure 2.25 and Figure 2.26. Since neither the PIV nor ADV can capture the data for the whole section, the corresponding data ranges are framed out in CFD results respectively.

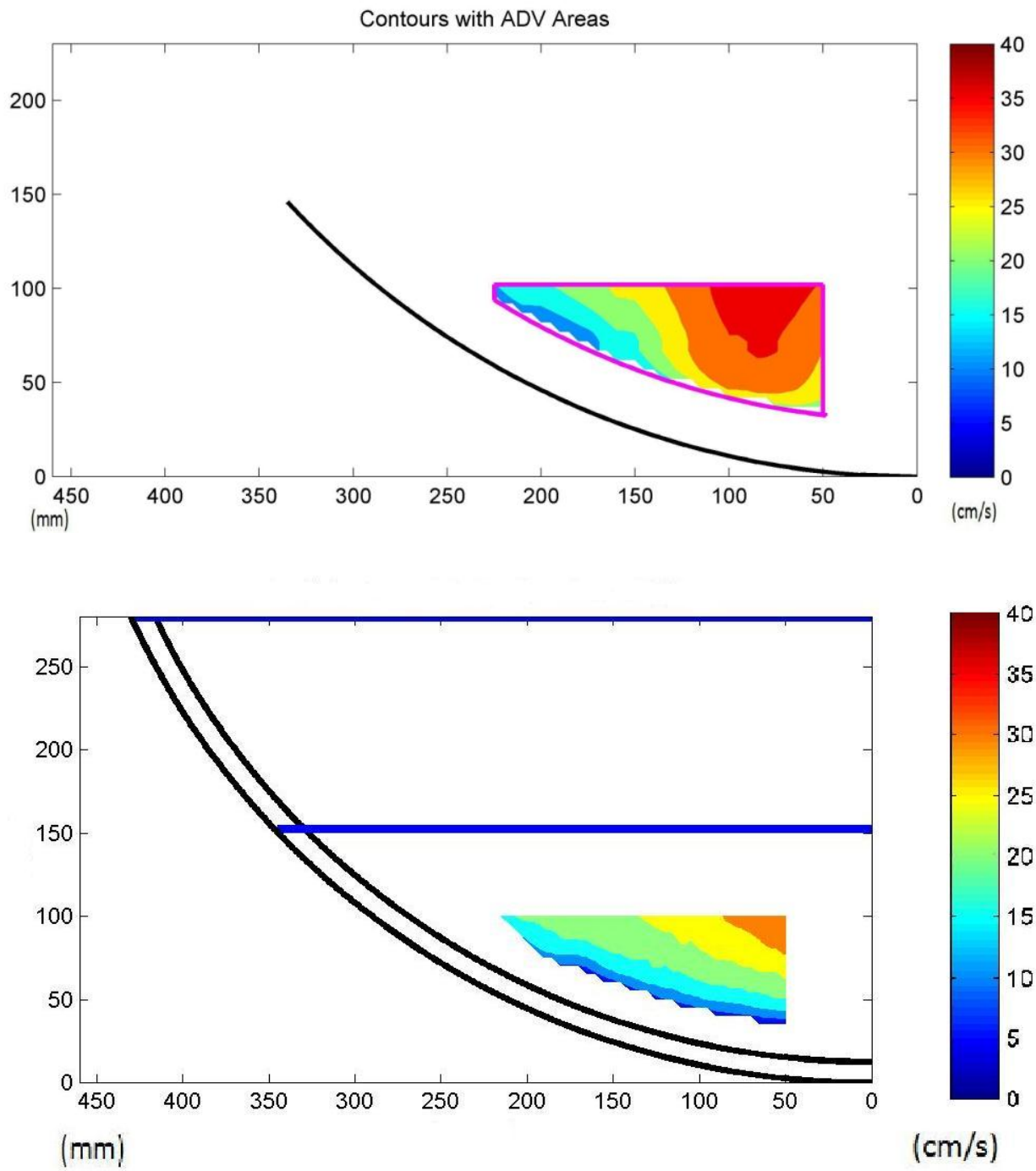

Figure 2.25: CFD velocity contour plot with ADV cut area (upper) vs. ADV velocity contour plot (lower) for 6 inch water depth on the trough section

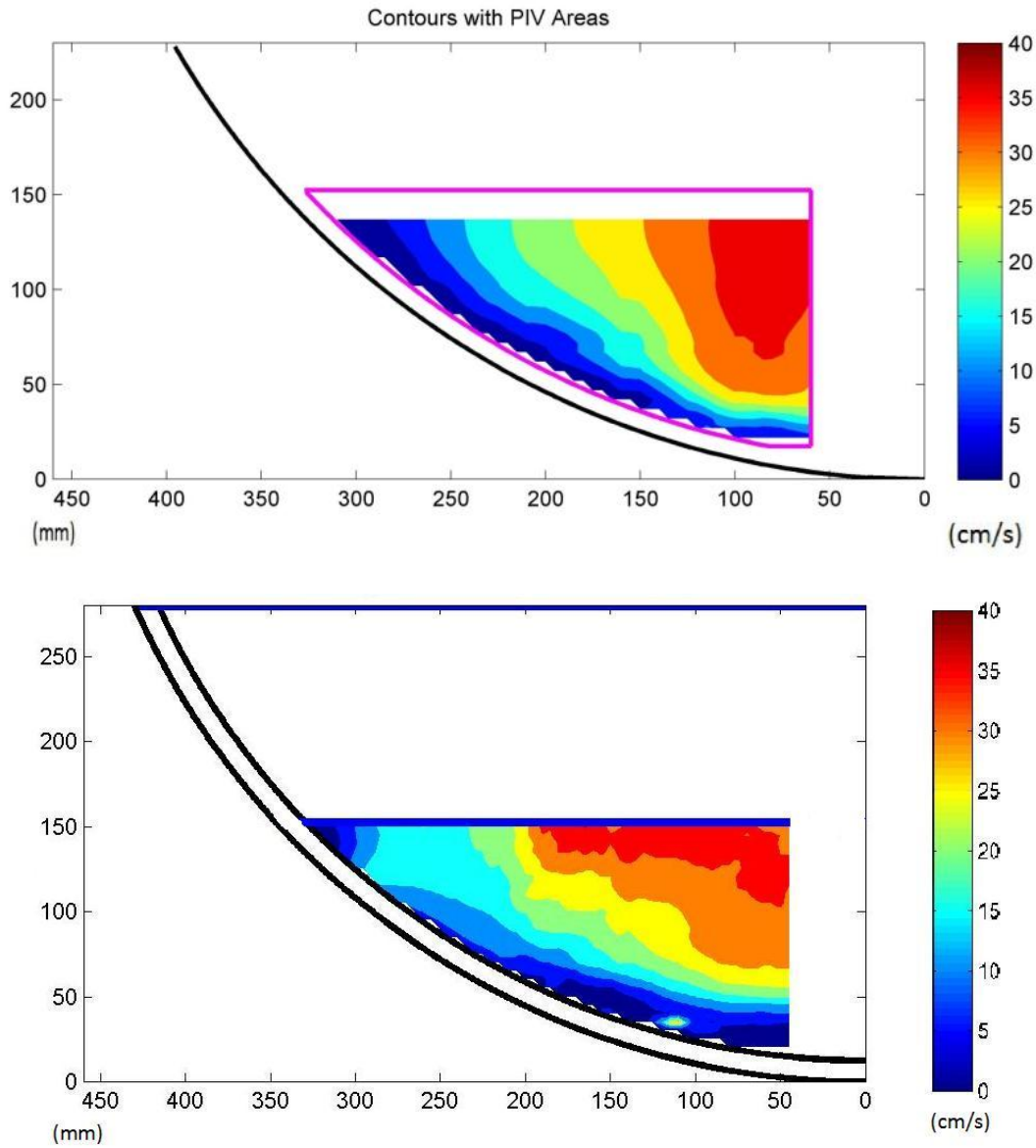

Figure 2.26: CFD velocity contour plot with PIV cut area (upper) vs. PIV velocity contour plot (lower) for 6 inch water depth on the trough section

The comparison between multi-phase CFD model results and ADV results for 9 inch water depth are shown in Figure 2.27, in which the comparable areas are much larger than those for 6 inch. The comparison of multi-phase CFD results and PIV results for 9 inch is still proceeding.

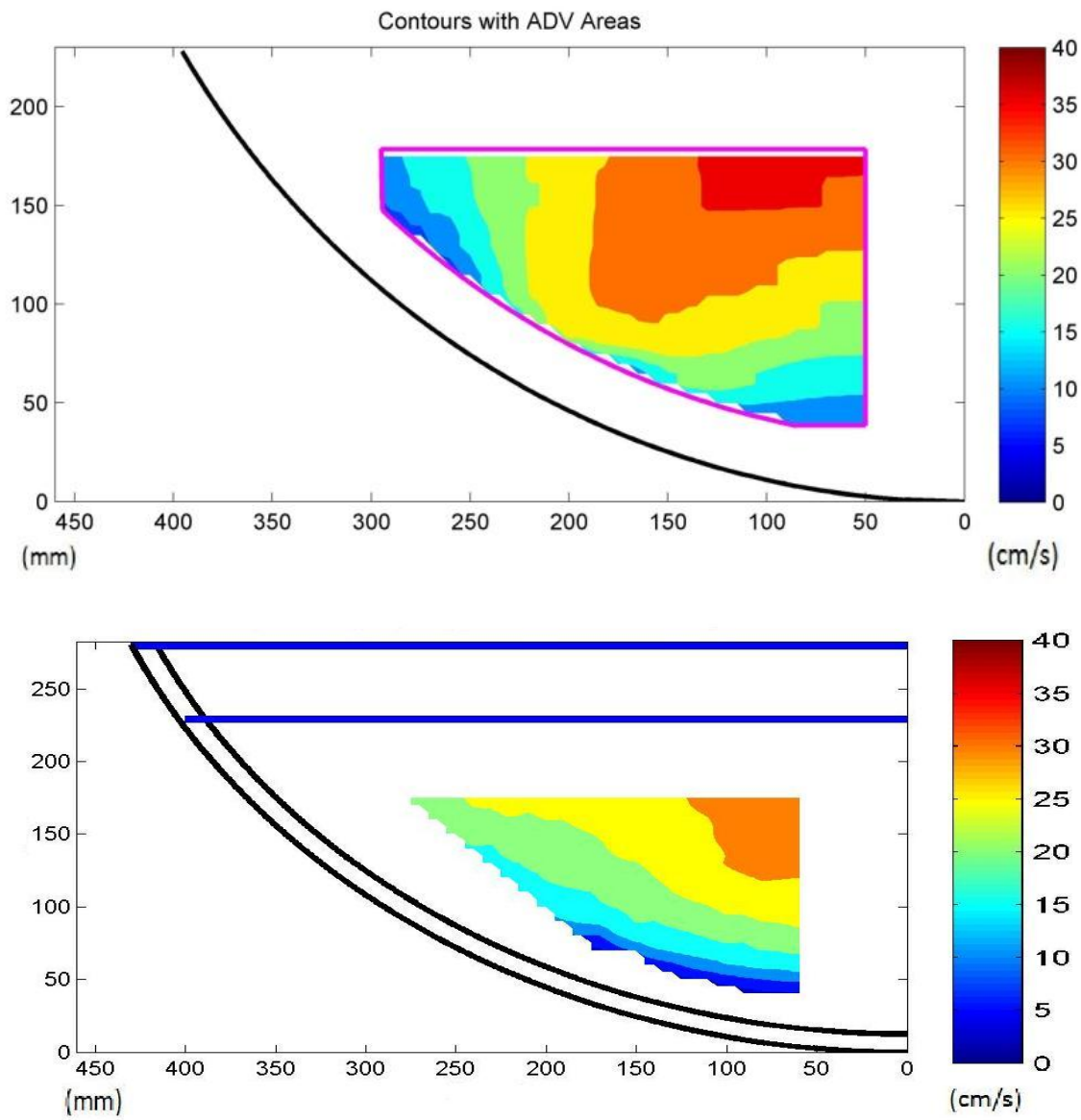

Figure 2.27: CFD velocity contour plot with ADV cut area (upper) vs. ADV velocity contour plot (lower) for 9 inch water depth on the trough section

The preliminary simulation results (for 0 bed elevation) reveal that the three-dimentional (3-D) two-phase (air and water) CFD models solved in STAR-CCM+ yield reasonably good agreement in the velocity distributions, compared with both the PIV and ADV data. The velocity distribution contours obtained from the CFD simulation are much closer to the PIV observation results. Furthermore, the PIV data capture range is larger than that of ADV because ADV can hardly get the data near the water surface and adjacent to the culvert boundary.

Note that the full flume single phase CFD model has better concurrence of velocity distribution with experimental measurements. Based on the discussion in Section 8.1.3.7, the single phase velocity

magnitude is larger than that of the multi-phase CFD model. Taking 90% of the magnitude of velocity obtained from the single phase CFD model, the visual agreement with the PIV results is presented in Figure 2.28.

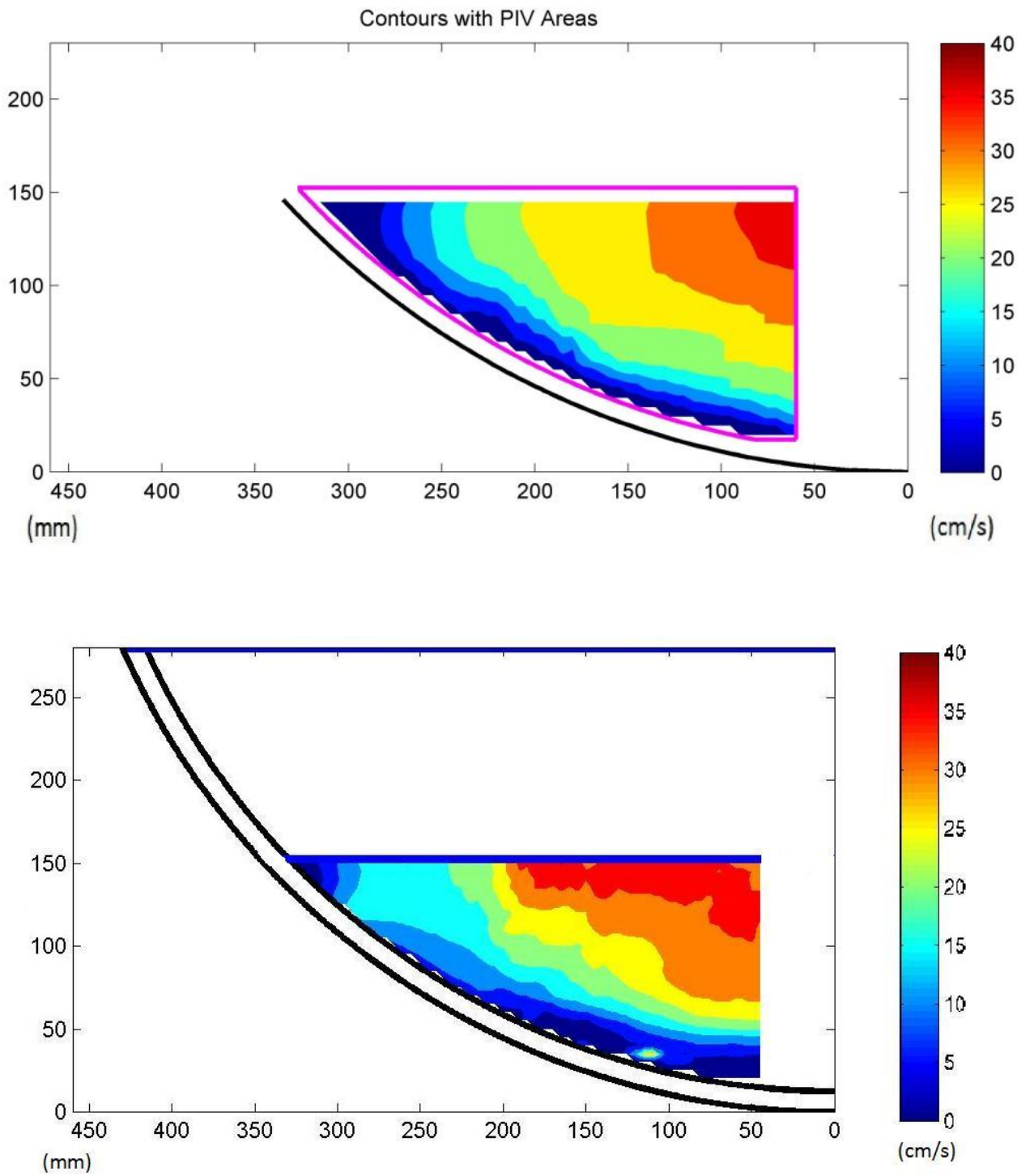

Figure 2.28: 90% single phase CFD velocity contour plot with PIV cut area from (upper) vs. PIV velocity contour plot (lower) for 6 inch water depth on the trough section

Conclusions for Comparison with Experiment: The experimental work is not yet complete, and therefore this assessment is preliminary. The experimental PIV and ADV data show differences that are of the same order as the differences between either of the experimental approaches and the CFD results. All of these show significant variation of velocity over culvert cross sections with higher velocity near the center. Making engineering use of data obtained from CFD analysis on cross section variation of velocity will likely be an improvement over just using the mean velocity in design of culverts for fish passage. While there are differences in both of the experimental techniques and the multiphase and single phase CFD approaches to obtaining the cross section velocity distribution, the information is much closer to reality than an assumed uniform mean velocity. Culvert design for fish passage cannot come close to conditions that would exhaust fish attempting to swim through the culvert, and therefore the use of data that has some uncertainty but is much better than current practice can still yield a major improvement in design practice.

2.3.9. References

1. Matt Blank, Joel Cahoon, Tom McMahon, "Advanced studies of fish passage through culverts: 1-D and 3-D hydraulic modeling of velocity, fish expenditure and a new barrier assesment method," Department of Civil Engineering and Ecology, Montana State University, October, 2008 .
2. Marian Muste, Hao-Che Ho, Daniel Mehl,"Insights into the origin & characteristic of the sedimentation process at multi barrel culverts in Iowa", Final Report, IHRB, TR-596, June, 2010.
3. Liaqat A. Khan, Elizabeth W.Roy, and Mizan Rashid, "CFD modelling of Forebay hydrodyamics created by a floating juvenile fish collection facility at the upper bank river dam", Washington, 2008.
4. Angela Gardner, "Fish Passage Through Road Culverts" MS Thesis, North Carolina State University, 2006.
5. Vishnu Vardhan Reddy Pati, "CFD modeling and analysis of flow through culverts", MS Thesis, Northern Illinois University, 2010.
6. Kornel Kerenyi, "Final Draft, Fish Passage in Large Culverts with Low Flow Proposed Tests" unpublished TFHRC experimental and CFD analysis of culvert flow for fish passage work plan, 2011.

3. Computational Multiphysics Mechanics Applications

3.1. Multiphysics Simulation of Salt Spray Transport

The Turner Fairbank Highway Research Center (TFHRC) currently is interested in studying the transport of salt spray generated by vehicle tires from the pavement up to the exposed steel support beams of steel bridges as the tires roll over wet pavement. The research is aimed to update the Technical Advisory, which is already over 20 years old, with results based on current state-of–the-art computational analysis and experimental data acquired at critical locations.

3.1.1. Estimate for Water Content in Semi-Trailer Truck's Wake

In [1], the modeling of the transport of salt-water mixture from the pavement surface to the underside of steel bridges was shown to involve three phases. The first phase is the lifting of the salt-water mixture from the road surface by the tires and ejecting the mixture into the swirling air around the wheels. The second phase is the egression of the mixture from the wheel region to the outside of the vehicle and from the under carriage of the vehicle, with eventual egression from the rear of the vehicle. Here the mixture will be referred to as a cloud, which is the vortex wake of the vehicle driving over a wet roadway (Figure 3.1). The third phase is the impact of a second vehicle—which is following the first vehicle—into the cloud and the potential transport of a portion of the cloud onto the steel beams.

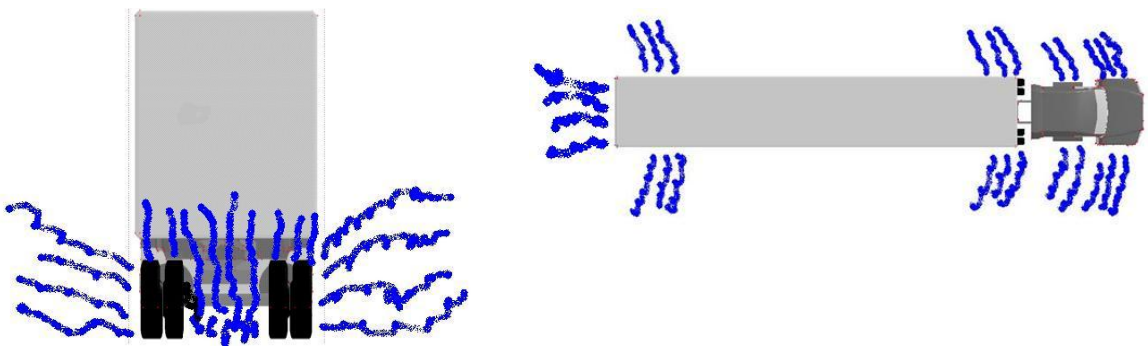

Figure 3.1: Egression of the salt-water air mixture into the air outside of the vehicle forming two side-of-vehicle clouds and a rear undercarriage cloud [1]

Up to now, most of the work done at the Transportation Research and Analysis Computing Center (TRACC) was to develop tractable models and modeling techniques for the MM-ALE approach. During this time, the entire air domain was assumed to be just air without any water content. This study estimates the water content of the resulting cloud formed during the second phase based on computational fluid dynamics (CFD) simulation results presented in [3] and presents recommended values for densities to be used for the cloud material in future simulations.

3.1.1.1. Approach

To date, an initial search of the literature did not turn up any experimental results for the water content in the vehicle wake, and this is unfortunate because experimental test data adds credibility to simulation results. However, a paper [3] based on numerical simulations using the STAR-CD software contains results that could be used in our LS-DYNA MM-ALE simulations.

In [3], spray dispersion simulations using a simplified semi-trailer model—the Generic Conventional Model (GCM)—were performed. Two cases were considered: without trailer-mounted base flaps and with trailer-mounted base flaps. Because the droplet sizes could range from 0.01 mm to 1 mm (0.0003937 inch to 0.03937 inch) this would entail an extremely large number of droplets on which to perform calculations, so a "parcel" approach was adopted. In the parcel approach, each parcel/particle represents a collection of droplets with a fixed mass. For our MM-ALE approach, this is ideal because we are not modeling droplets but are modeling the movement of multiple materials (air, cloud, and vehicle) through a fixed computational mesh. So we are interested in the mass properties of each of these materials in order to compute their movement under, around and over the bridge as the truck travels under the bridge and displaces the air and cloud.

3.1.1.2. Results

In [3], two designs were considered for the trailer: without trailer-mounted base flaps and with trailer-mounted base flaps. The flaps were shown to have an effect on the distribution of the parcels in the trailing wake (cloud). Figure 5, p. 12 in [3] shows the parcel distribution obtained for the case without flaps and with flaps, respectively.

A close study of those graphics shows that for the case with flaps the parcels tend to be lower and rise to approximately one-third to one-half the height of the trailer. In contrast for the case without flaps, the particles rise to the top and possibly above the top of the trailer. The importance of this observation is that a trailing vehicle (car or truck) then has the potential to push these parcels up higher—perhaps between the bridge's beams. Another observation is that the mean diameter of most of the parcels appears to be 0.54 mm (0.02126 inches) or less.

In [3] a 13 meter long by 5 meter wide by 3.3 meter high (42.6 ft. by 16.4 ft. by 10.83 ft.) sampling domain was used, and the number of parcels in the domain was computed for the two cases. Note, one parcel contains 22.2 grams of water (0.0485 lb.). A conversion from parcels to mass was performed for the two cases, and the results are shown in Table 3.1.

Table 3.1: Water content in sampling domain generated by a GCM traveling at 29 m/s (65 mph) [1]

Without Trailer-Mounted Flaps		With Trailer-Mounted Flaps	
2.15 parcels/m^3	0.0609 parcels/ft^3	3.4 parcels/m^3	0.0963 parcels/ft^3
48.375 g/m^3	0.00295 lb/ft^3	76.5 g/m^3	0.00467 lb/ft^3

The density of water is 1,000 kg/m^3, and for the case without flaps the mass per cubic meter is 48.375 g; so the volume of the water is 48.375 * 10-6 m^3. For the case with flaps case, the volume of water is 76.5 * 10-6 m^3.

For an initial analysis, it is assumed that the parcel distribution is uniform throughout the sampling domain. The density of air at sea level and 15 degrees Celsius is 1225.21 g/m^3. So for the case without–flaps, the combined mass of the air and water in a cubic meter is 1273.59 grams, and for the case with-flaps, it is 1301.71 grams. Table 3.2 shows the resulting densities that should be used for the cloud material in the MM-ALE simulations. The ratio of the density of the cloud to the density of air, which is seen to be from 4% to 6% larger than that of the air alone, appears to be reasonable.

Table 3.2: Cloud material densities generated by a GCM traveling at 29 m/s (65 mph)

Trailer-Mounted-Flaps	Without	With
Mass of air plus water (g)	1273.59	1301.71
Density (g/m^3)	1273.59	1301.71
Density ratio	1.039	1.062

Looking at **Error! Reference source not found.**, the parcels are concentrated near the lower third (approximately) of the sampling domain. So for this case, the density would be higher. By considering all the parcels to be located in the lower third of the sampling box, the density of the cloud, becomes 19 % greater than air.

3.1.1.3. Discussion and Recommendations

Based on prior simulations reported in Reference [3], an estimate of the water content in the cloud (i.e., the trailing vortex wake) of a semi-trailer truck was made. Reference [3] used a sampling box to collect data on the distribution of parcels (i.e. a collection of water droplets) behind the semi-trailer for the case where the trailer had flaps and the case without flaps. Our initial estimate for TRACC's calculations assumed a uniform distribution within the sampling box and showed that the density of the cloud was between 4-6% higher than air. Thus, adjusting the density of the material representing the cloud by these values would give a fair engineering representation for the cloud behavior in the MM-ALE simulations. Using the uniform distribution assumption with a 4-6% increase in cloud density is a reasonable perturbation that should not generate any numerical surprises in the simulation runs.

Examining the figure showing parcel distribution within the bounding box for the case with flaps shows that most of the parcels appear to be in the bottom third of the box. Thus, when the assumption of uniform distribution is relaxed, and a higher distribution near the lower third of the box is made, the density would be 19% higher than the density of air. A close study of the graphics shows that for the case with flaps the parcels tend to be lower and rise to approximately one-third to one-half the height of the trailer. In contrast for the case without flaps, the particles rise to the top and possibly above the top of the trailer. The importance of this observation is that a trailing vehicle (car or truck) then has the

potential to push these parcels up higher—perhaps between the bridge's beams. Another observation is that the mean diameter of most of the parcels appears to be 0.54 mm (0.02126 inches) or less.

Another issue that needs to be addressed is the appropriate equation of state for the cloud material. For simulations performed to date, a polynomial equation for air was used because only the air was modeled. When moisture is considered along with the air at a density of 4-6 % greater than air, engineering judgment is to use the equation of state for air for the cloud but to use the higher densities. For a cloud density of 19% greater than air, additional thought needs to be given on the appropriate equation of state, and this will be presented in a future work.

During this past winter season, TRACC CSM staff made personal observations of the trailing wake (cloud) of semi-trailers on I88 while traveling at 105 kmph (65 mph). The qualitative observation was that the bulk of the salt spray reached about 2.5 meters (8 feet) high—a little over the top of the car. Subsequently, during this spring's rainy season, similar observations were made on a local highway while traveling at 80 kmph (50 mph), and it appeared that the spray reached the top of the trailer (4.1 m/13.5 ft.). It is apparent that the cloud configuration will depend on the semi-trailer truck and the specific shape of the tractor, trailer, undercarriage features, etc.

It is recommended that field data be obtained for the water distribution in a cloud to complement numerical simulations. Perhaps, movies could be taken alongside and behind a semi-trailer to qualitatively get an idea of the size of the cloud. This could be done in the winter time when road salt is present. In addition during the summer/fall, water could be spread over a short stretch of highway—say two to three trailer lengths long—and video cameras could be positioned along the roadway to record the cloud behavior as a semi-tractor trailer traveled over the wet pavement. To enhance cloud visibility, the water could be colored or black screens could be positioned on the side of the roadway opposite to the video recorders. This experiment could be done on the open road and under a bridge.

The beginning of a quantitative assessment could be made by developing a device that could be mounted on the front of a small truck and would collect water at different Y-Z locations (Y is in the direction transverse to the truck, and Z is in the vertical direction) behind a semi-trailer truck for a length of time equal to a distance of 13 m, which is the length of the sampling domain used in [3]. This data could be compared to the simulation results reported in [3] and also would be of value, in and of itself.

3.1.1.4. References

1. Kulak, R. F., Application of Multiphysics Mechanics to Modeling Salt Spray Transport onto Steel Support Beams of Bridges, RFK Engineering Mechanics Consultants, Technical Note: TRACC-TFHRC-001, November 13, 2010.
2. Kulak, R. F., Feasibility Study on using MM-ALE Approach to Modeling Salt Spray Transport onto Steel Support Beams of Bridges, RFK Engineering Mechanics Consultants, Technical Note: TRACC-TFHRC-002, December 02, 2010.
3. Paschkewitz, J. S., Simulation of Spray Dispersion in a Simplified Heavy Vehicle Wake, Lawrence Livermore National Laboratory, UCRL-TR-218207, January 17, 2006.

3.1.2. Simulation of a Semi-trailer Truck Passing Through a Bridge Underpass

Based on the recent study, a finite element model of the Raleigh - Tamarack Overpass (Bridge No. 4172) was updated. The domain of the air over the truck was significantly extended to minimize the effect of the boundaries on the flow of the air around the vehicle and the bridge beams. The model is shown in Figure 3.2. The main area of interest is built of hexahedral elements with edge size of 100 mm (darker blue area in the drawing). The rest of the domain is built of elements that increase in size further out from the vehicle. The basic statistics of the model are listed in Table 3.3.

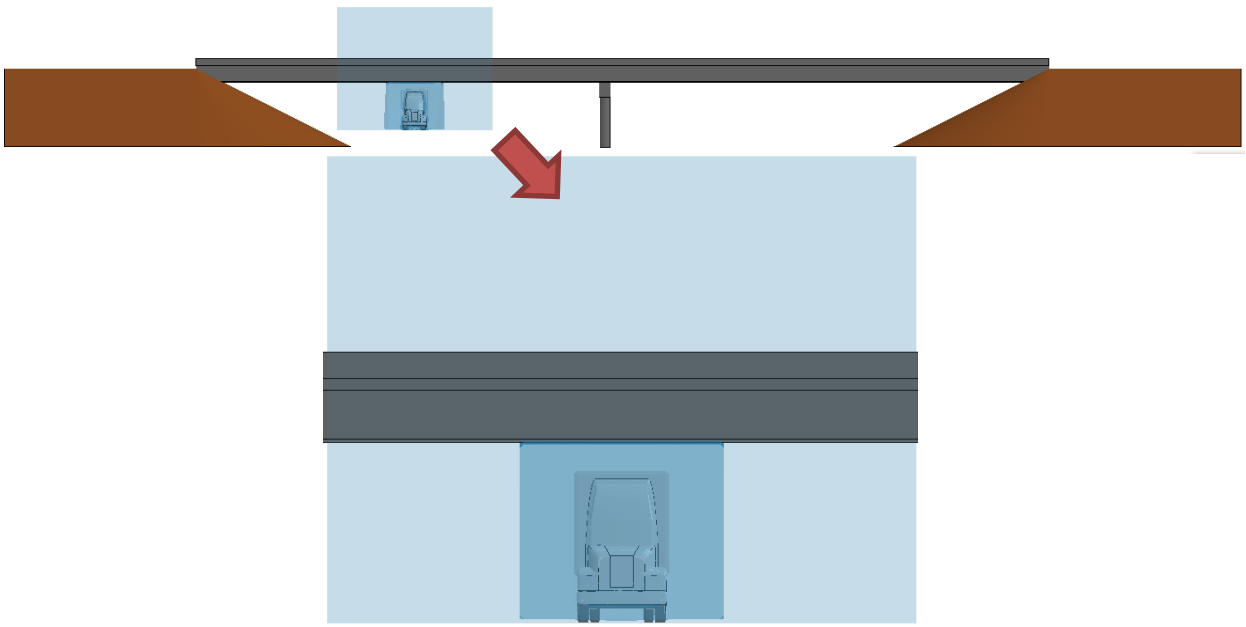

Figure 3.2: Setup for analysis of the air movement under the bridge

Table 3.3 Statistics of the FE model of the bridge

Entity	Count
Number of Nodes	4,622,267
Number of Shell Elements	829,082
Number of Solid Elements	3,774,363
Number of Deformable Solids	3,301,688
Total number of elements	4,603,445

The simulation was performed for 3.0 seconds of real time, which took about 72 compute-hours to complete. Several quantities were tracked in the simulations for visualization of the results. The most important quantities were the spatial trajectories of tracer particles in the air. They represent virtual, massless particles that follow precisely the flow of the air. A three-dimensional matrix of tracer particles was defined in the volume before and under the overpass. The particles were defined in horizontal planes at four vertical levels:

- the wheel level,
- the engine level
- the windshield level
- the top surface of the trailer level

Nine cross sections in the travel direction were defined, and at each vertical level in each cross section, five tracer particles were defined in the direction perpendicular to the travel direction. This provided the ability to study the motion of the air as the truck moves through the underpass. Overall there were 180 tracer particles defined.

For each level, the figures below show the particle trajectories at different times in the simulation. In addition, velocity isosurfaces are shown on each of the figures to provide a look at the motion of the air as the truck passes through the underpass. Figure 3.3 shows trajectories of the particles at the level of the wheel axles. Most of the particles stay at this level except for the ones being trapped behind the cabin. These trapped particles can be lifted up and dragged by the vehicles for long distances.

In Figure 3.4, the trajectories of the particles at the engine hood level are shown. The particles that are along the mid-width of the vehicle are lifted up from the hood level to the trailer-top level and are dragged along with the vehicle. The particles away from the mid-width of the vehicle are pushed to the sides of it and are not lifted higher.

In Figure 3.5, the trajectories of the particles located at the windshield level are shown. These particles are also smoothly pushed up to the top surface of the trailer. Once the particles get to the back of the trailer, they become part of the developing vortex wake. This causes the particles to move down rapidly and follow the back of the trailer – i.e., the particles are entrapped in the trailer's vortex wake. Eventually, some of the particles exit from the wake and appear to move into the space between the bridge beams. The particles at the trailer's top-surface-level behave in a similar way (see Figure 3.6); they also appear to find their way into the space between the bridge beams.

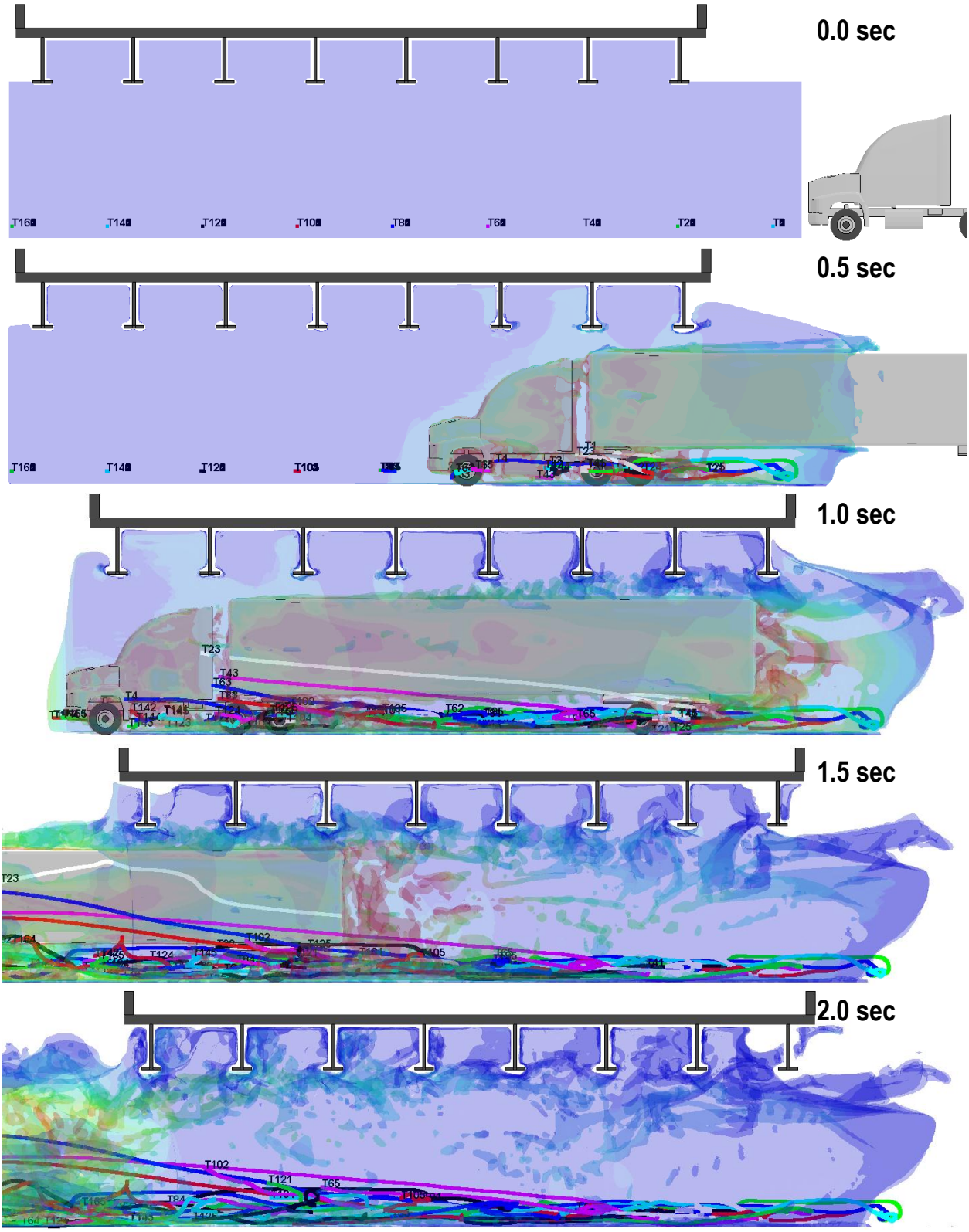

Figure 3.3: Behavior of tracer particles at the level of the wheel axis

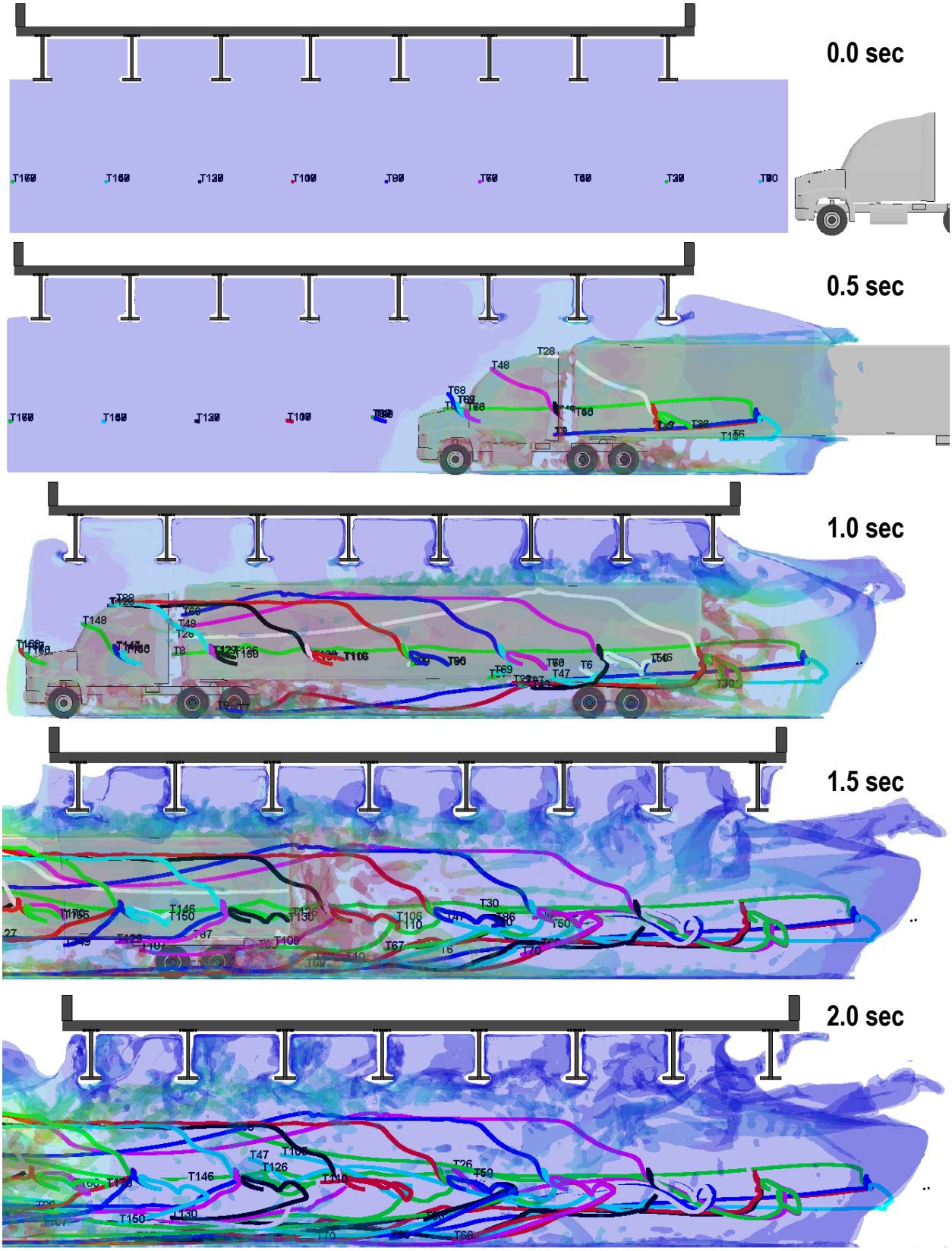

Figure 3.4: Behavior of tracer particles at the level of the engine hood

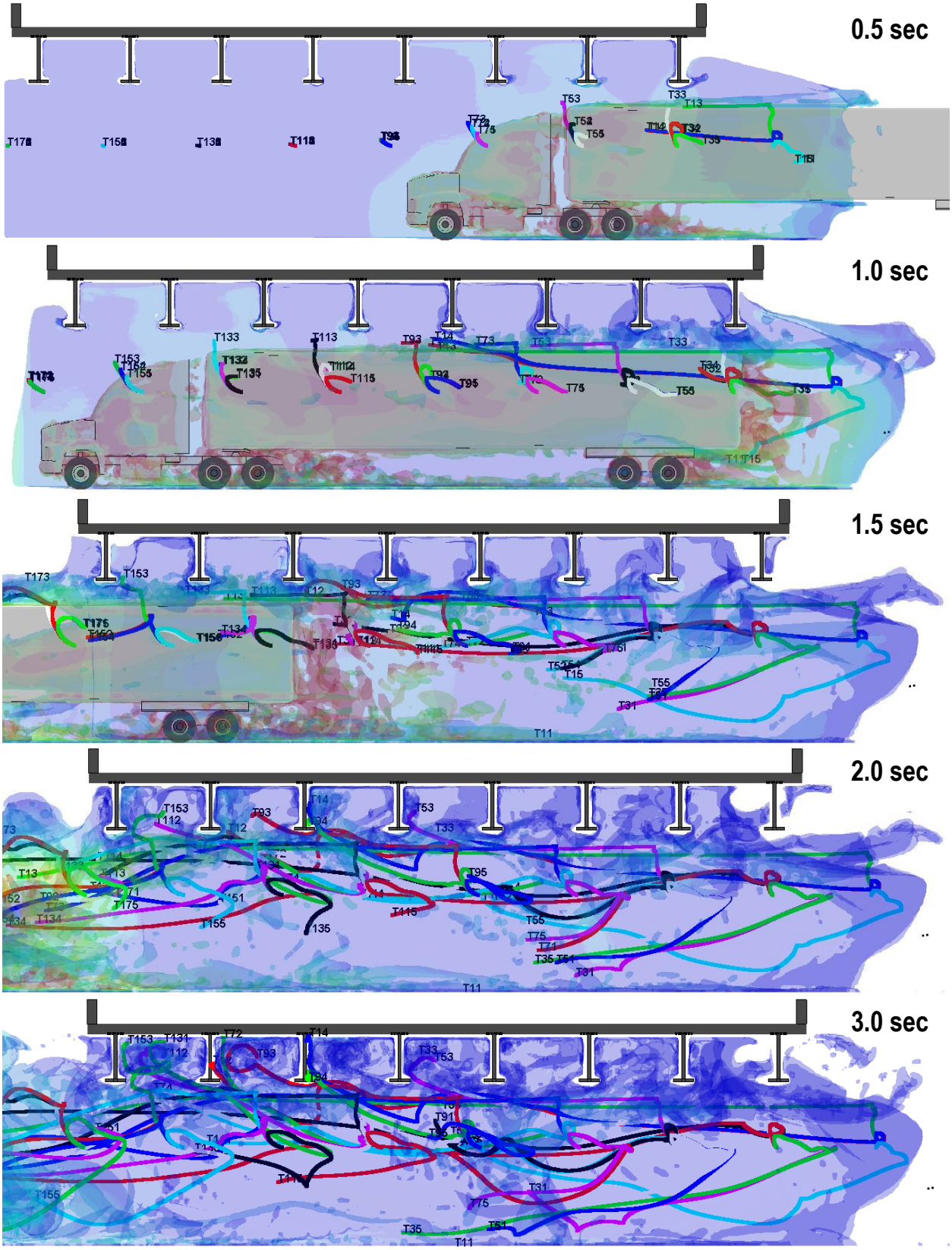

Figure 3.5: Behavior of tracer particles at the level of the windshield

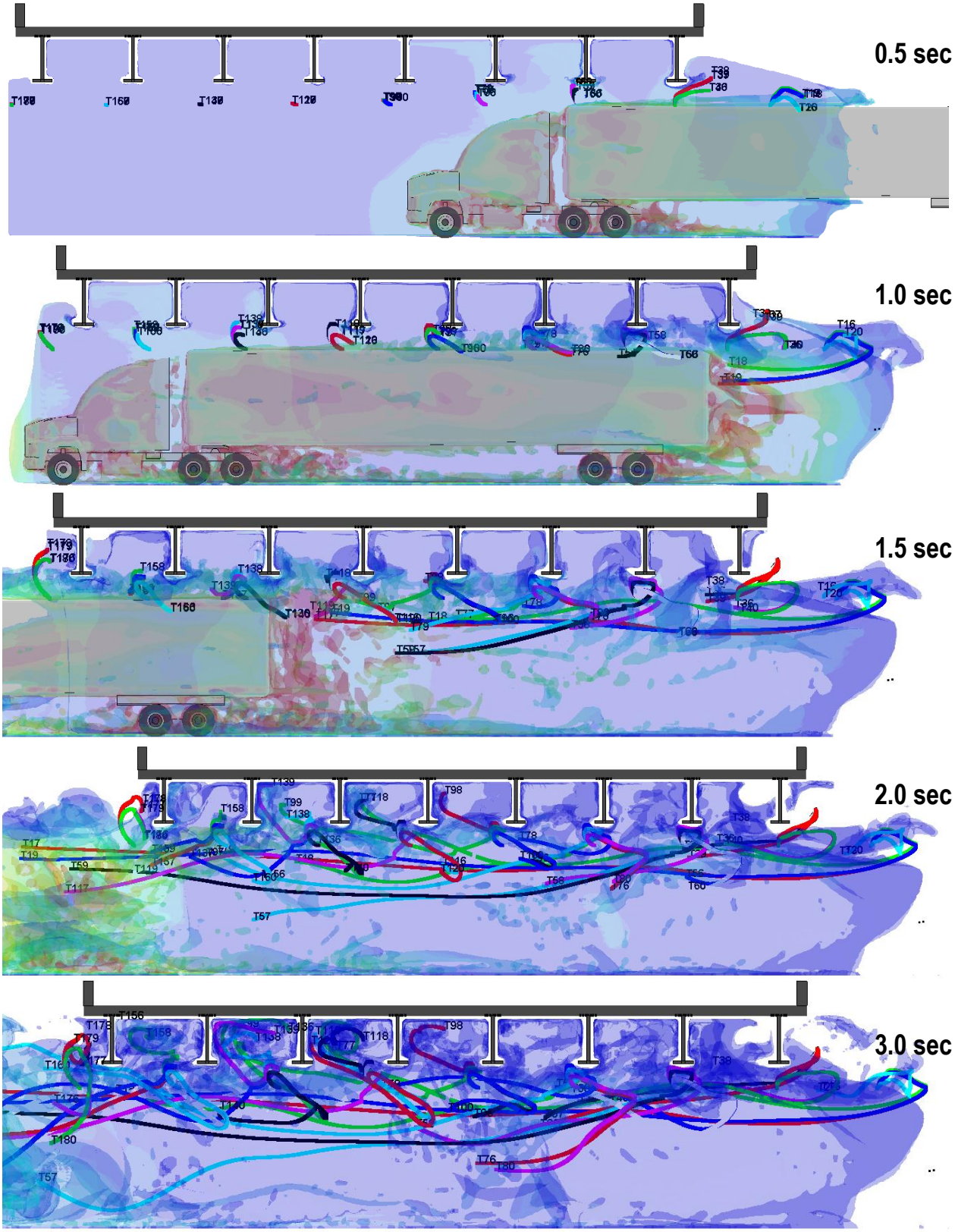

Figure 3.6: Behavior of tracer particles at the level of the top surface of the trailer

Next, the air motion between the beams as the truck passes under the bridge is studied. Velocity vector plots with superimposed velocity isosurfaces are presented to understand the motion. A typical plot is shown in Figure 3.7 where the small arrows show the velocity at a specific instant of time. Because these vectors are difficult to see, a large red arrow is superimposed on the plots to show the general movement of the air in a given region. Figure 3.8 shows the middle cross section – i.e., the area perpendicular to the direction of truck motion -- through the air domain and velocity vectors together with the velocity isosurfaces. At 0.5 sec, the vehicle is approaching this cross section, and the air is starting to move up. At 1.0 sec, when the vehicle is passing under this cross section, the air on the top part of the domain behaves in a similar way. Increased velocities can be seen in the proximity of the vehicle wheels and around the trailer. At 1.5 sec, the vehicle is past this cross section, and the velocity vectors have changed directions. Now they are pointing downward, and as mentioned previously, the air is sucked down to the vacuum created behind the truck. With time, the vectors continuously change their directions. It is important to note that this mechanism could potentially cause transport of the air containing the water-salt spray from the road surface to the bridge beams.

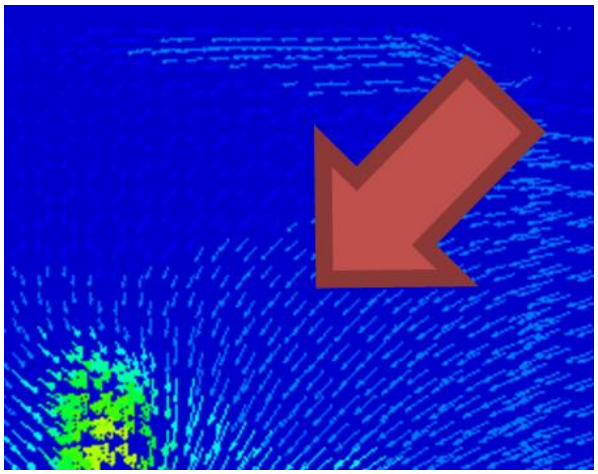

Figure 3.7: Close up view of the velocity vectors

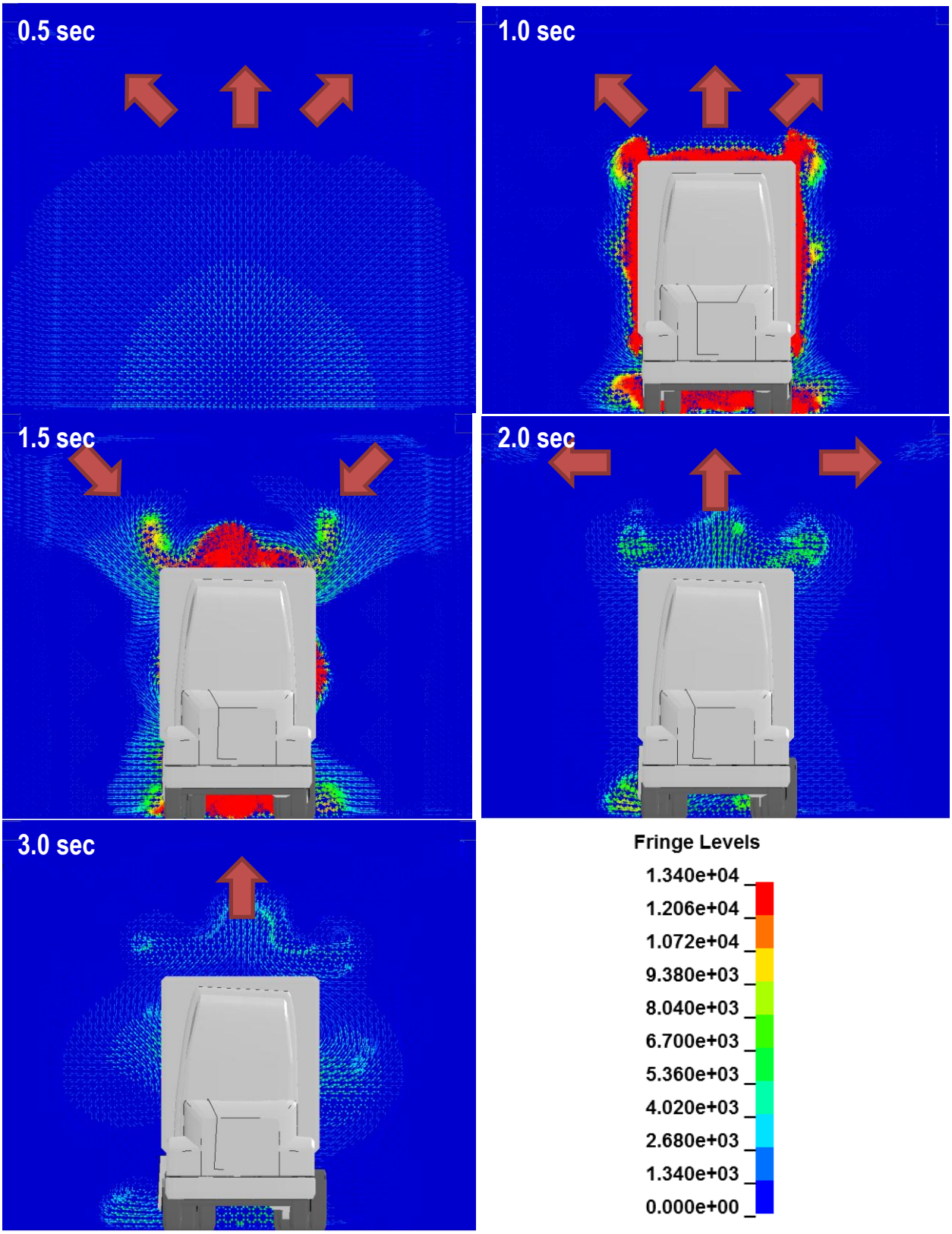

Figure 3.8: Velocity vectors in the middle cross section of the air domain

The present work is a first look at the behavior of the air under a bridge as a semi-trailer truck passes through the underpass: therefore, it must be considered very preliminary. It was assumed that the air was stationary and the truck was moving at 60 mph. Stable calculations were performed up to 3 seconds of simulation time, which allowed the truck to enter and completely pass under the bridge.

In looking over the results, it is beneficial to divide the simulation into two phases. The first phase looks at the air motion as the air approaches and passes around the semi-trailer truck; the second phase considers the air motion after the truck has passed – i.e., the motion of the air behind the truck. During the first phase, it was seen that the air moves over, under and around the sides of the truck. Simulations showed that the air particles originally at the level of the top of the trailer – i.e., the highest level that was traced to date – appear to move to the flange area around the bottom of the beams. They do not appear to reach the web of the beams or the bottom of the bridge deck. Perhaps, particles originally at the level of the flanges could be pushed higher into the space between the beams.

Examining the air motion during the second phase reveals some interesting behavior. During this phase, complex wake vortices develop behind the vehicle from the four edges of the trailer. To a first order, the simulations appear to capture this motion; however, at this time there is uncertainty associated with the accuracy. Keeping this in mind, results show that the air originally at the mid-height of the windshield or higher can be transported into the spaces between the bridge beams.

The results from computational fluid dynamics simulations performed by Lawrence Livermore National Laboratory (see Section 3.1.1) showed that the road surface water can be propelled up to at least to the height of the top of a semi-trailer by the trailer's vortex wake. In view of this, a second semi-trailer truck would now be passing through the first trailer's vortex wake that potentially contains a mixture of air and salt water at levels near the top of the trailer, which could then be propelled between the beams.

In the next quarter, it is planned to continue studies using the current model. The following cases will be considered:

- A truck traveling through an air domain without a bridge;
- A truck traveling through an underpass with a vertical embankment close to the traffic lane;
- A truck traveling through an underpass with a vertical embankment close to the traffic lane and larger distance between the trailer top and bottom of the bridge beams;
- Additional runs of the above cases using two trucks – a leading truck and a trailing truck.

Finally, the details of the trailing vortex wake will be studied.

3.2. Wind Engineering

The work presented in this section was performed by graduate students at Northern Illinois University under the partial guidance of the CSM staff.

3.2.1. Vehicle Stability under High Wind Loadings

3.2.1.1. Literature Review

The previous quarterly report presented the dynamic equation of motions for a truck with forward velocity and external loading (wind force). As the formulation of equations was complex due to incorporation of various body parts of the truck, there was a necessity for simplification of the previous model.

In order to get a clear understanding of the dynamic behavior of a truck, a model with three rigid bodies as sprung mass, front axial and rear axial (Figure 3.9) was used [1]. The equations of the model were simpler compared with the previous version as it excludes the compliance of other parts. The equations of the truck with three rigid bodies are given as follows [1]:

$$m_s * h * \ddot{\phi} = -m * U * (\dot{\beta} + \dot{\psi}) + Y_\beta * \beta + Y_{\dot{\psi}} * \dot{\psi} + Y_\delta * \delta \tag{3.1}$$

$$-I_{\acute{x}\acute{z}} * \ddot{\phi} + I_{\acute{z}\acute{z}} * \ddot{\psi} = N_\beta * \beta + N_{\dot{\psi}} * \dot{\psi} + N_\delta * \delta \tag{3.2}$$

$$\begin{aligned} I_{\acute{x}\acute{x}} * \ddot{\phi} - I_{\acute{x}\acute{z}} * \ddot{\psi} \\ &= m_s * g * h * \phi - m_s * U * h * (\dot{\beta} + \dot{\psi}) - k_f * (\phi - \phi_{t,f}) - l_f * (\dot{\phi} - \dot{\phi}_{t,f}) \\ &+ u_f - k_r * (\phi - \phi_{t,f}) - l_r * (\dot{\phi} - \dot{\phi}_{t,r}) + u_r \end{aligned} \tag{3.3}$$

$$\begin{aligned} -r * (Y_{\beta,f} * \beta + Y_{\dot{\psi},f} * \dot{\psi} + Y_{\delta,f} * \delta) \\ &= m_{u,f} * U * (h_{u,f} - r) * (\dot{\beta} + \dot{\psi}) + k_{t,f} * \phi_{t,f} - m_{u,f} * g * h_{u,f} * \phi_{t,f} - k_f \\ &* (\phi - \phi_{t,f}) - l_f * (\dot{\phi} - \dot{\phi}_{t,f}) + u_f \end{aligned} \tag{3.4}$$

$$\begin{aligned} -r * (Y_{\beta,r} * \beta + Y_{\dot{\psi},r} * \dot{\psi}) \\ &= m_{u,r} * U * (h_{u,r} - r) * (\dot{\beta} + \dot{\psi}) + k_{t,r} * \phi_{t,r} - m_{u,r} * g * h_{u,r} * \phi_{t,r} \\ &- k_r * (\phi - \phi_{t,r}) - l_r * (\dot{\phi} - \dot{\phi}_{t,r}) + u_r \end{aligned} \tag{3.5}$$

Where,

r = height of roll axis, measured upwards from ground

u = active roll torque

l = suspension roll damping rate.

k =suspension roll stiffness

k_b = vehicle frame torsional stiffness

k_t = tire roll stiffness

k_ϕ = vehicle coupling roll stiffness

k_ψ = vehicle coupling yaw stiffness

ϕ = absolute roll angle of sprung mass.

ϕ_t = absolute roll angle of unsprung mass

$I_{\acute{x}\acute{x}}$ = roll moment of inertia of sprung mass, measured about origin of coordinate system

$I_{\acute{x}\acute{z}}$ = yaw-roll product of inertia of sprung mass, measured about origin of coordinate system

$I_{\acute{z}\acute{z}}$ = yaw moment of inertia of total mass, measured about origin of coordinate system

$N_\beta = \frac{\partial M_z}{\partial \beta}$ = partial derivative of net tire yaw moment with respect to sideslip angle.

$N_{\dot{\psi}} = \frac{\partial M_z}{\partial \dot{\psi}}$ = partial derivative of net tire yaw moment with respect to yaw rate.

$N_\delta = \frac{\partial M_z}{\partial \delta}$ = partial derivative of net tire yaw moment with respect to steer angle.

m_s= Sprung mass,

h = height of center of sprung mass, measured upwards from roll center

m = total mass

U = forward speed

$\dot{\psi}$= yaw rate

$Y_\beta = \frac{\partial F_y}{\partial \beta}$ = partial derivative of net tire lateral force with respect to sideslip angle

β = sideslip angle

$Y_{\dot{\psi}} = \frac{\partial F_y}{\partial \dot{\psi}}$ = partial derivative of net tire lateral force with respect to yaw rate

$Y_\delta = \frac{\partial F_y}{\partial \delta}$ = partial derivative of net tire lateral force with respect to steer angle

δ = steer angle

These equations could be effectively solved using the state space method. Mathematical expression of state space representation model is as follows [1]:

$$\dot{x} = A * x + B_0 * u + B_1 * \delta$$

Where,

x = $[\beta \quad \dot{\psi} \quad \phi \quad \dot{\phi} \quad \phi_{t,f} \quad \phi_{t,r}]^T$

u = $[u_f \quad u_r]^T$

$$E = \begin{bmatrix} m * U & 0 & 0 & m_s * h & 0 & 0 \\ 0 & I_{\acute{z}\acute{z}} & 0 & -I_{\acute{x}\acute{z}} & 0 & 0 \\ m_s * U * h & -I_{\acute{x}\acute{z}} & 0 & I_{\acute{x}\acute{x}} & -l_f & -l_r \\ -m_{u,f} * U * (h_{u,f} - r) & 0 & 0 & 0 & -l_f & 0 \\ -m_{u,r} * U * (h_{u,r} - r) & 0 & 0 & 0 & 0 & -l_r \\ 0 & 0 & 1 & 0 & 0 & 0 \end{bmatrix}$$

$$A = E^{-1} \begin{vmatrix} Y_\beta & Y_{\dot{\psi}} - m * U & 0 & 0 & 0 & 0 \\ N_\beta & N_{\dot{\psi}} & 0 & 0 & 0 & 0 \\ 0 & -m_s * h * U & m_s * g * h - k_f - k_r & -l_f - l_r & k_{t,f} & k_{t,r} \\ r(Y_{\beta,f}) & r(Y_{\dot{\psi},f}) + m_{u,f} * U * (h_{u,f} - r) & -k_f & -l_f & k_f + k_{t,f} - m_{u,f} * g * h_{u,f} & 0 \\ r * (Y_{\beta,r}) & r * (Y_{\dot{\psi},r}) + m_{u,r} * U * (h_{u,r} - r) & -k_r & -l_r & 0 & k_r + k_{t,r} - m_{u,r} * g * h_{u,r} \end{vmatrix}$$

$$\begin{bmatrix} 0 & 0 & 0 & 1 & 0 & 0 \end{bmatrix}$$

$$B_0 = E^{-1} \begin{bmatrix} 0 & 0 & 1 & 0 & 1 & 0 \\ 0 & 0 & 1 & 1 & 0 & 0 \end{bmatrix}^T$$

$$B_1 = E^{-1} \quad [Y_\delta \quad N_\delta \quad 0 \quad r * Y_{\delta,f} \quad 0 \quad 0]^T$$

3.2.1.2. Conversion of wind velocity to wind pressure

The conversion of wind velocity to wind pressure is necessary because the wind is described in terms of velocity and in the finite element analysis the velocities are attached to the nodes and pressure is applied to elements. The loading on elements would provide more accurate results compared to the node loading.

The pressure due to wind velocity can be computed using the following conversion:

$$P = 0.5 * C * D * V^2$$

Where,

P = Pressure (N/m^2)

C = Drag coefficient

D = Density of air (1.25 Kg/m^3)

V = Speed of air (m/s)

The drag coefficient is a dimensionless quantity and it depends upon the surface area under the influence of attacking wind. The drag coefficients for flat and cylindrical body are approximated as follows:

Drag coefficient for flat surface = 1

Drag coefficient for cylindrical surface = 0.67.

3.2.1.3. Development with the FEM

After understanding the spring-damper system in LS-DYNA, it was necessary to study the motion of a node on a surface. To perform the analysis, a flat surface was created with two beam element and two massless nodes attached to it (Figure 3.10). These nodes were given a velocity and constraint so as to follow the beam element from start to end.

With the success to the above analysis, a spring element was attached to the nodes and a block was mounted on it (Figure 3.11). To verify the proper behavior of the spring, an initial displacement was given and it produced the appropriate result.

After verifying the behavior with the above model, the task was to give an appropriate loading to the vertical face of block in order to understand the effects of wind pressure (Figure 3.12). Two types of wind pressure were given to the block, a constant load and a sine load.

The properties of the model are:

Mass = 5.88 Kg,

Stiffness = 60 N/mm,

Length of spring = 50 mm,

Amplitude = 0.01,

Frequency = 100 Hz,

Forcing function = Amplitude*SIN(2*3.14*Frequency*TIME)

Figure 3.13 shows the graph of horizontal displacement of the block with the application of sinusoidal wave as a forcing function.

Theoretically, the equation of motion of the block with vertical springs and horizontal sine forcing function (Figure 3.12) is given by:

$$m\ddot{x} + k\frac{x^2}{\sqrt{l^2 + x^2}} = F_0 \tag{3.6}$$

Where,

m = Mass of the block,

k = Stiffness of spring,

l = original length,

x = Displacement from static equilibrium position

F_0 = Forcing function (sine wave)

3.2.1.4. Ford F-800 truck development

A Ford F-800 truck model (Figure 3.14) was taken from the National Crash Analysis Center (NCAC) website [2]. The raw file contained a FEM model of the truck with six rigid walls attached to each tire and forward velocity. This model was studied and modified according to the requirements of the

analysis. The basic modifications consist of creating a new rigid wall which was attached with the body of the truck, changing the forward velocity, and applying damping and pressure load (Figure 3.15).

Damping Estimation:

In order to gain a clear understanding of the behavior of the truck, the truck was made stationary (no forward velocity). Initially the truck was ideally modeled and to simulate the actual environmental condition, the truck model was allowed to settle on its suspensions. The displacement graph of the ideal truck is shown in (Figure 3.16). The graph contains displacement of three nodes from which the third node shows a clear displacement and it was used for further analysis. The displacement graph gives the properties of the suspension and the results of applying a global damping value to the system.

The damping estimation for LS-DYNA is calculated as follows:

$$D = 2 * \omega_{min} \tag{3.7}$$

$$\omega_{min} = \frac{2 * \pi}{T} \tag{3.8}$$

Where,

T = Time period between two successive crest or troughs of the displacement graph (Figure 3.16).

D = critical damping factor.

The displacement graph gives the value as follows:

T = 0.25 seconds

This reflects,

$D = 50.24 \ \ N - s/mm$

Various damping values below the critical damping value from 20 to 45 in multiples of 5 were given to the model. An optimum damping value was chosen in order to stabilize the truck and further application of wind load was possible without the effect of a global damping factor. Figure 3.17 gives the displacement obtained from various damping values.

3.2.1.5. Wind Loading

A wind pressure loading was given to the side of the trailer part of the truck. When a pressure was given with the help of conventional way (load_segment) it was seen that the pressure remains exactly perpendicular to the surface irrespective of the trailer position. This was contradicting with the actual situation as the wind loading should be along the ground surface. This actual situation was simulated in the model by developing a wind load with the help of the load_segment_nonuniform keyword

command. This requires the creation of a local co-ordinate system and the load directed with the help of directional cosines.

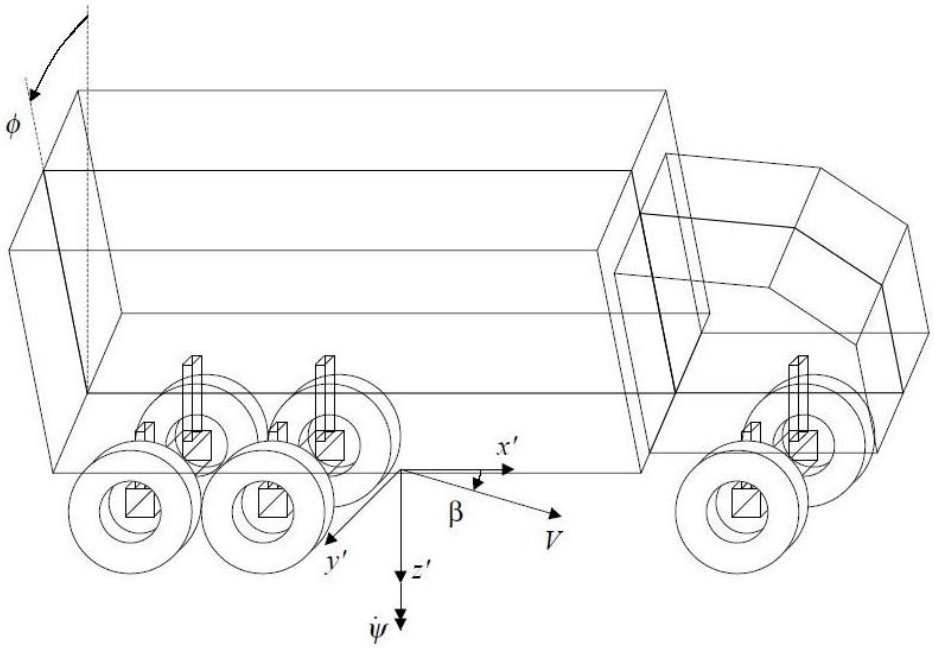

Figure 3.9: Single unit rigid vehicle [1]

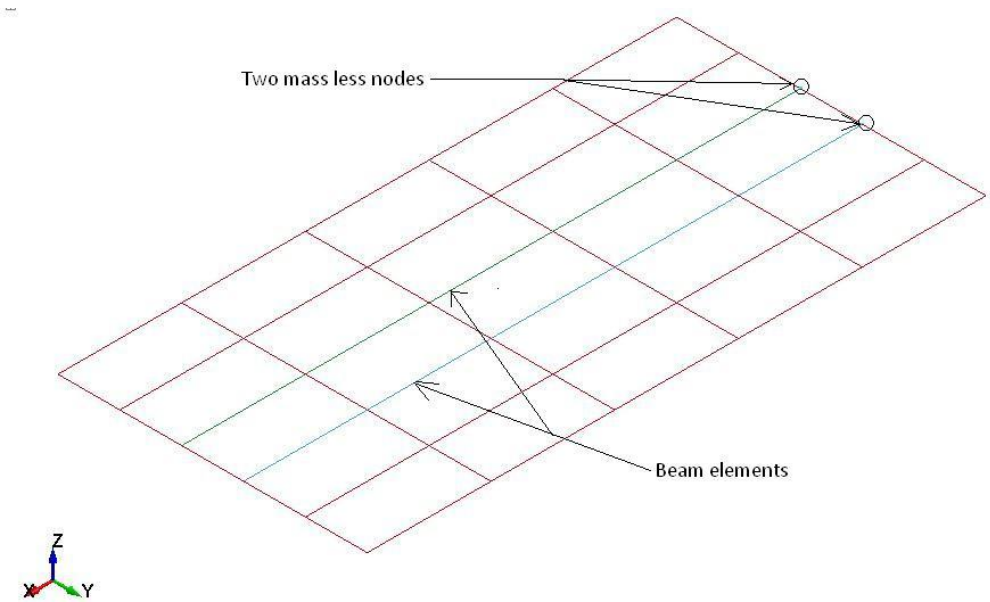

Figure 3.10: Mass-less nodes moving on a beam element

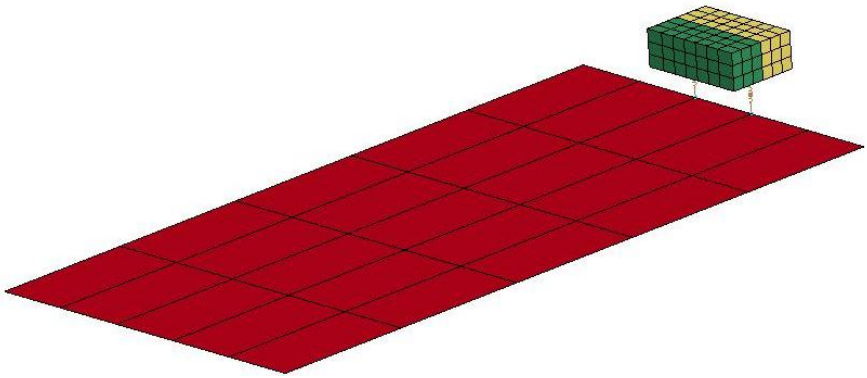

Figure 3.11: Motion of block attached with spring elements

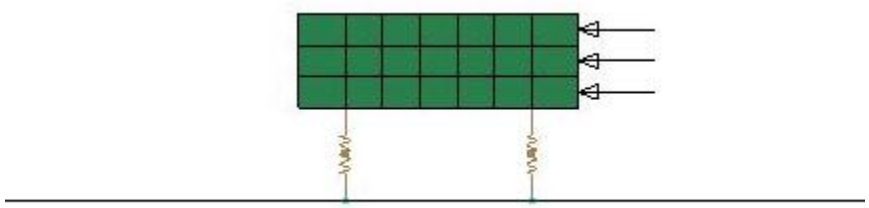

Figure 3.12: Wind loading applied at the side of the block

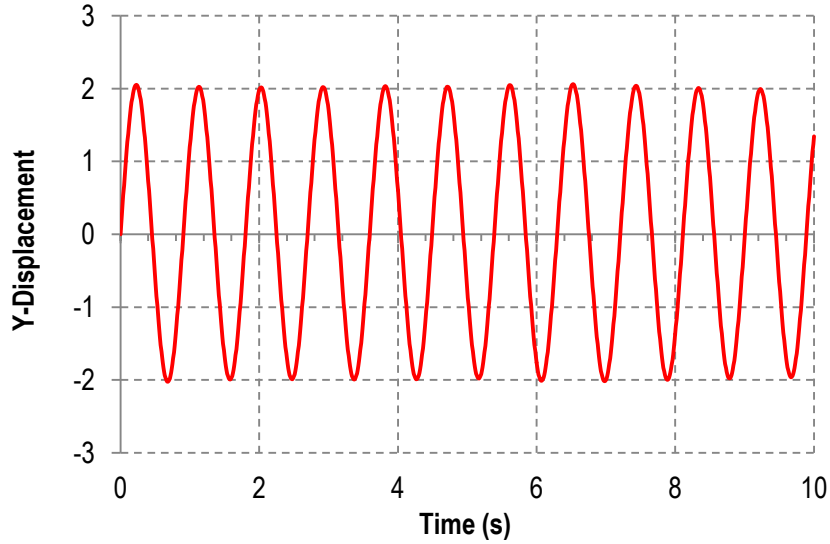

Figure 3.13: Displacement graph of block model with vertical springs and horizontal load

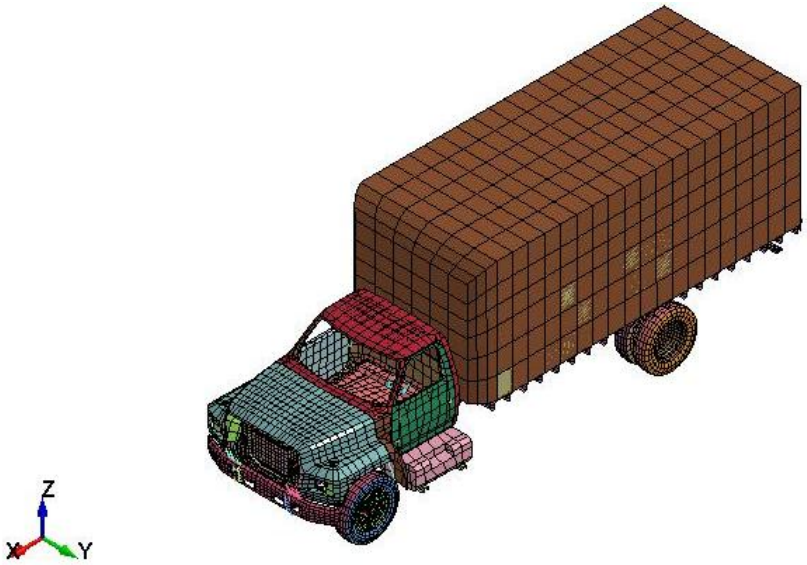

Figure 3.14: FEM Model of a Ford F-800 truck obtained from NCAC [2]

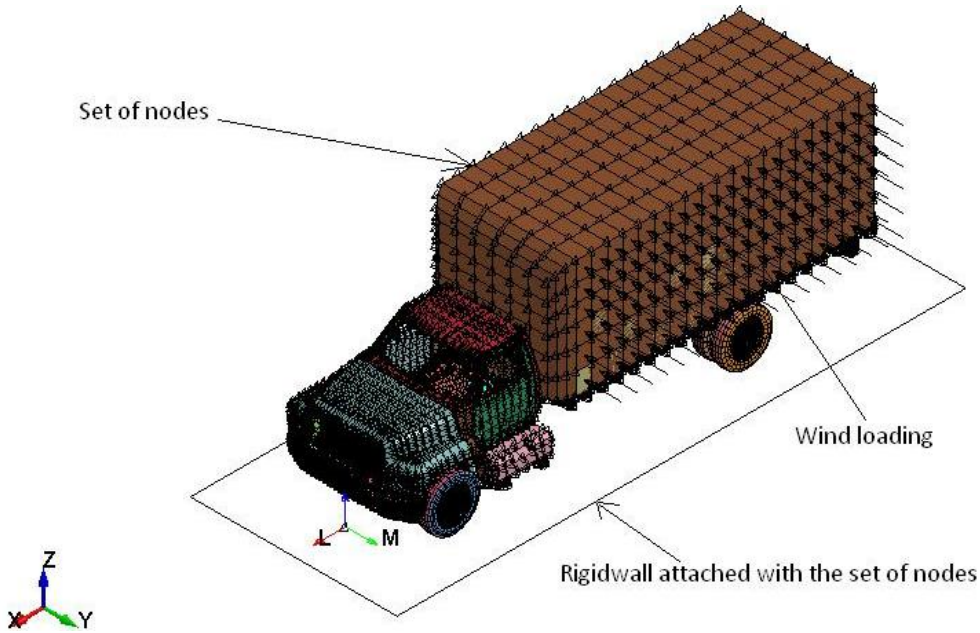

Figure 3.15: FEM model modified according to the analysis

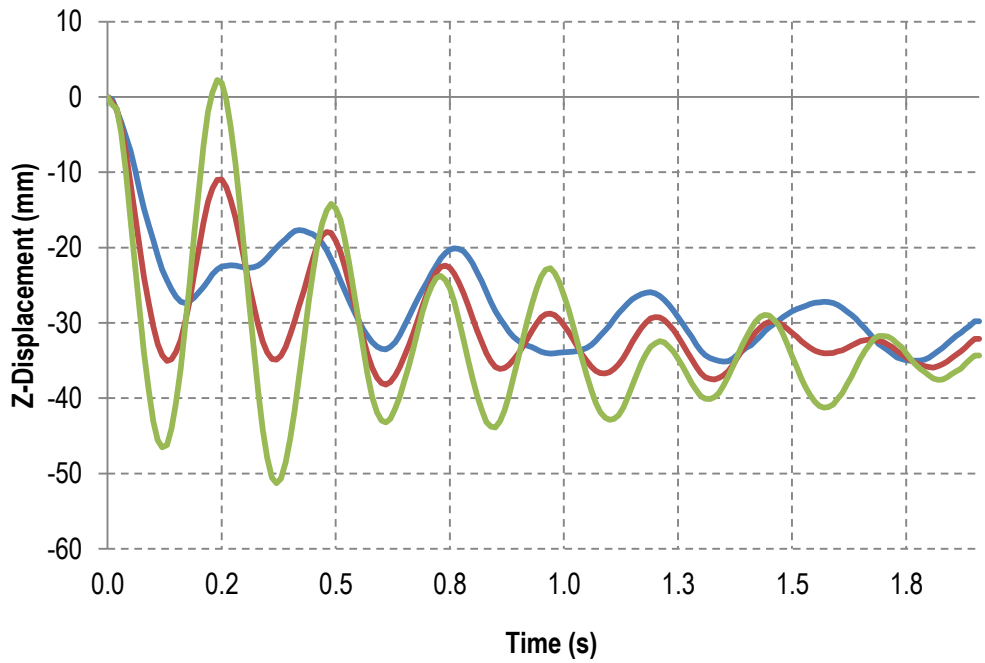

Figure 3.16: Graph of free displacement of truck on the suspension

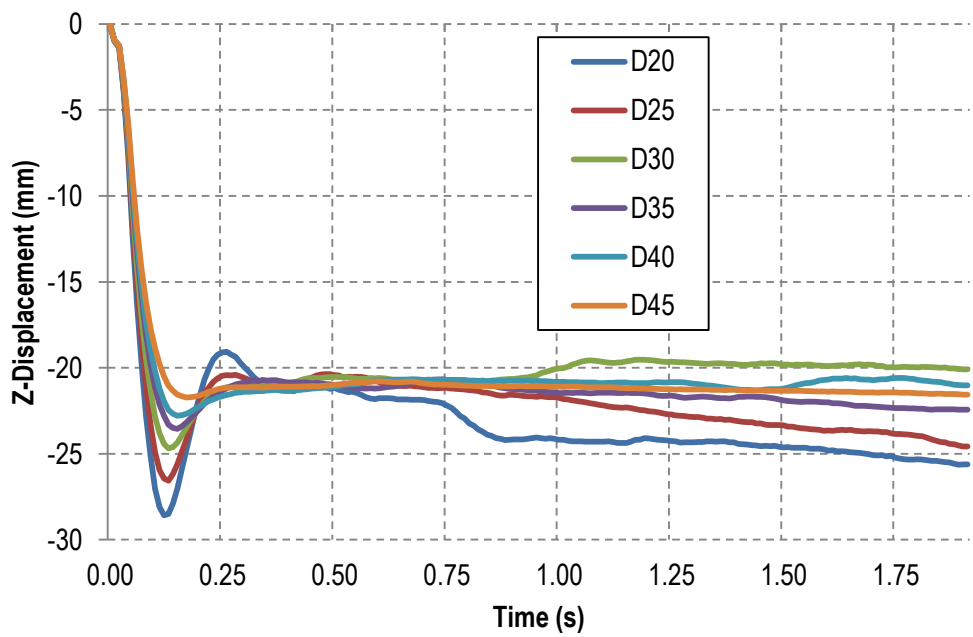

Figure 3.17: Displacement graph of various damped values

3.2.1.6. References

1) Sampson, D. J. M., "Active Roll Control of Articulated Heavy Vehicles", A dissertation for the Degree of Doctor of Philosophy, submitted to the University of Cambridge, September 2000.
2) http://www.ncac.gwu.edu/

3) Chen, F. and Chen, S., "Assessment of vehicle safety behavior under adverse driving conditions"; 11th American Conference on wind loading, San Juan, Puerto Rico, June 22-26, 2009.
4) Winkler C.B. and Ervin R.D., "Rollover of heavy commercial vehicles", UMTRI-99-19, The University of Michigan, Transportation Research Institute, Michigan, August 1999.

3.2.2. Electromagnetic Shock Absorber for Vehicle Stability under High Wind Conditions

New work done during the third quarter involved the analytical modeling of the electromagnetic shock absorber (EMSA) as well as its incorporation into the ¼ car Simulink model. The Simulink model utilizes an actual road profile as the disturbance for the system and the data is automatically exported into Microsoft Excel for post-processing. Also, FEM simulations of the Ford F800 truck model were performed to obtain mass, stiffness and damping properties.

3.2.2.1. New EMSA Model

The new analytical model of the EMSA is based upon [1]. The operation of this EMSA is very similar to the original proposed model. The main difference is that this new model utilizes two permanent magnet (PM) assemblies surrounded by a moving coil assembly mounted to a sliding armature [1]. When the coil assembly moves in and out of the PM assemblies, a voltage is produced in the coils.

In order to provide control over the EMSA, a voltage input is calculated based upon the relative velocity seen by the EMSA and the desired force. The desired force is calculated based upon the four states of the ¼ car model, [see Equation (8.14) from the previous TRACC Quarterly Report (Y5Q2)]. The actual force of the EMSA does not exactly match the desired force, since the EMSA force is limited by the direction of the generated voltage. In other words, the input voltage must be in the same direction as the generated voltage.

The induced or generated voltage in each coil section is:

$$V_{gen} = 2\pi rnh\dot{X}_1 B_i \tag{3.9}$$

Where r is the radius of the coil assembly, n is the number of turns per length, h is the height or length for the section, $\dot{X}_1$ is the relative velocity seen by the EMSA and B_i is the magnetic flux from the PM assembly. It is evident that the total length of wire for each coil section is:

$$L = 2\pi rnh \tag{3.10}$$

The force generated opposing the motion of the coil form is:

$$F = ILB_i \tag{3.11}$$

The circulating current in the coil assembly is denoted by I. The total voltage for each section of the coil assemblies is the summation of the generated voltage and the input voltage:

$$V_{total} = V_{gen} + V_{in} \tag{3.12}$$

The input voltage is determined by using ohms law, by substituting the total voltage divided by the resistance into Equation (3.11). After solving for the voltage input, the final equation takes the form:

$$V_{in} = F * \left[\frac{R}{L * B_i}\right] - \dot{X}_1 * [L * B_i] \tag{3.13}$$

The Simulink model that calculates the input voltage has conditional blocks that ensure the input voltage is in the same direction as the circulating voltage. If the input voltage is in the opposite direction of the circulating voltage, the conditional blocks set the input voltage to zero. The EMSA force for a given road profile is very similar to the desired force. Shown in Figure 3.18 is the desired force, which is based upon the states of the system. Shown in Figure 3.19 is the EMSA force, which is based upon the desired force, the relative velocity and the conditional blocks. The major difference between the two plots is that the EMSA force tends to dwell near zero due to the conditional statements. The gain values for the desired force were obtained from [2].

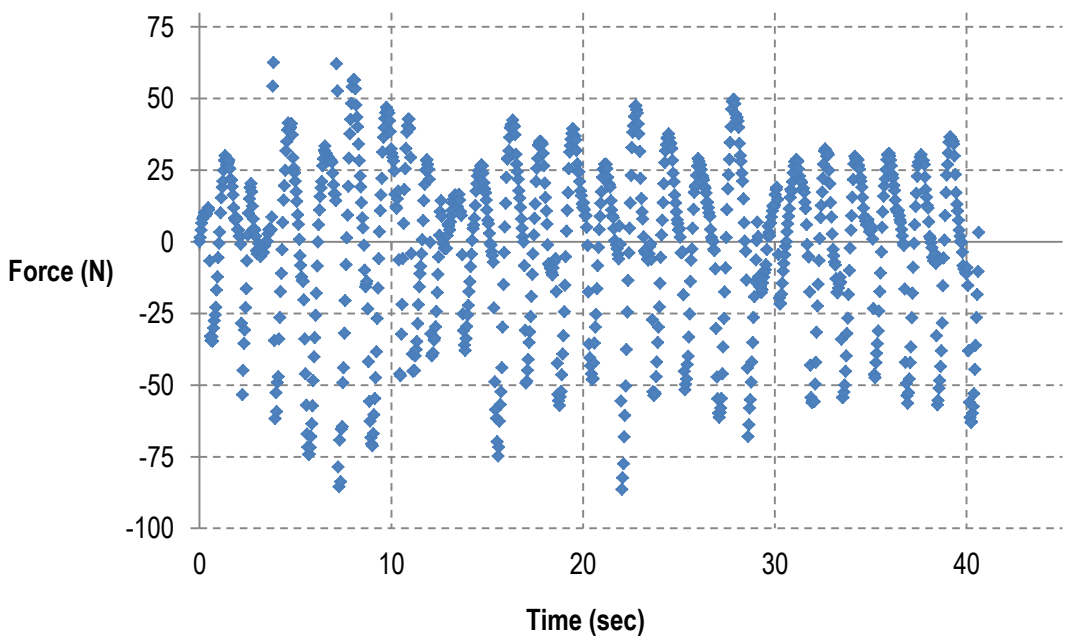

Figure 3.18: Plot of the Desired Force, based upon the states

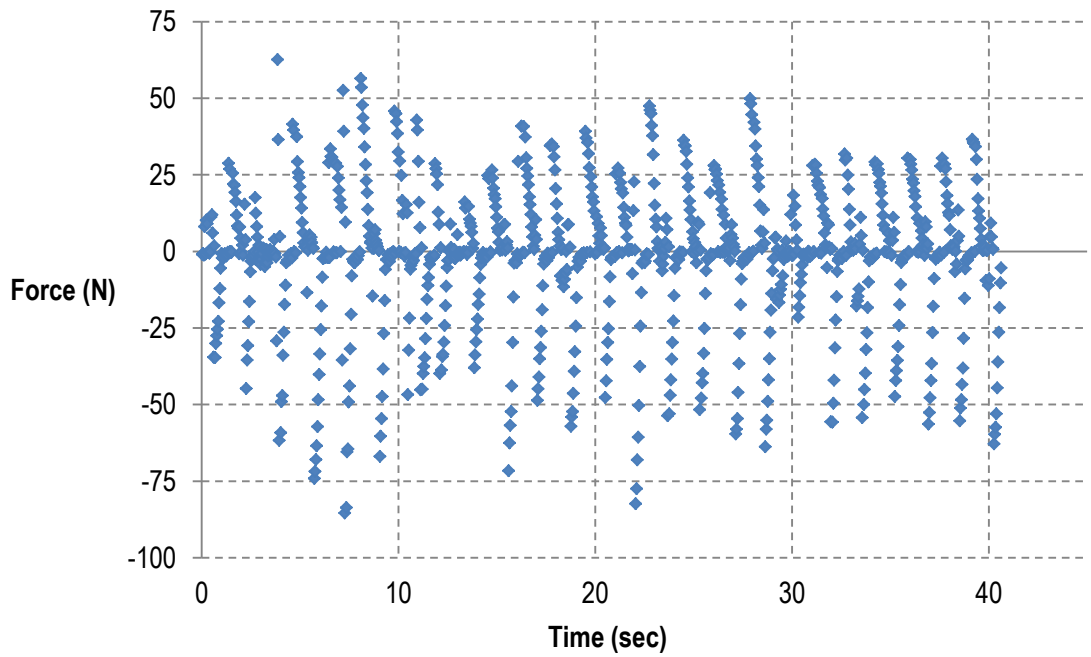

Figure 3.19: Plot of the EMSA force

3.2.2.2. Improved Simulink Model

The Simulink model now incorporates an actual road profile obtained from the Long Term Pavement Performance (LTPP) Department under the U.S. Department of Transportation Federal Highway Administration. The road profile is an array of data points, which are vertical deflection measurements. The measurements are separated by a distance of four feet. Shown in Figure 3.20 is a representation of the road profile data. However, the Simulink model needs the road profile data to be in terms of time. This is achieved by assuming the vehicle is traveling at a constant velocity. Shown in Figure 3.21 is the actual road profile plot used in the Matlab-Simulink model.

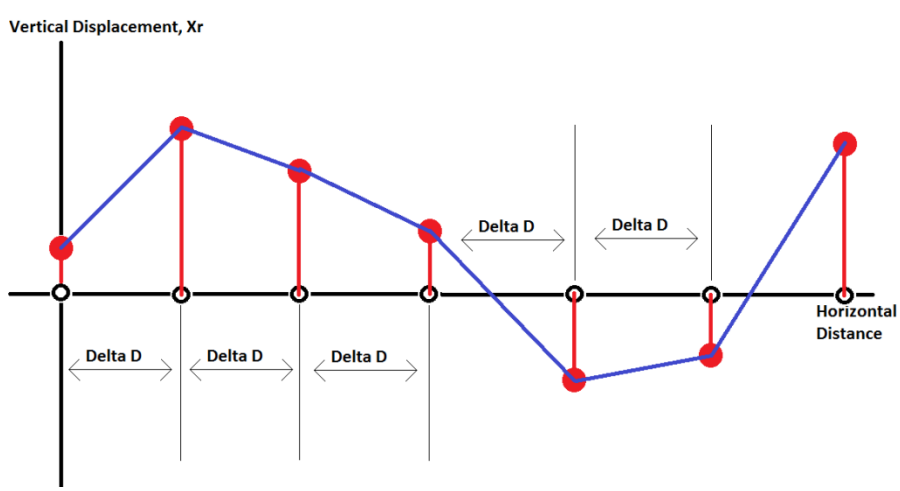

Figure 3.20: Schematic of the road profile data

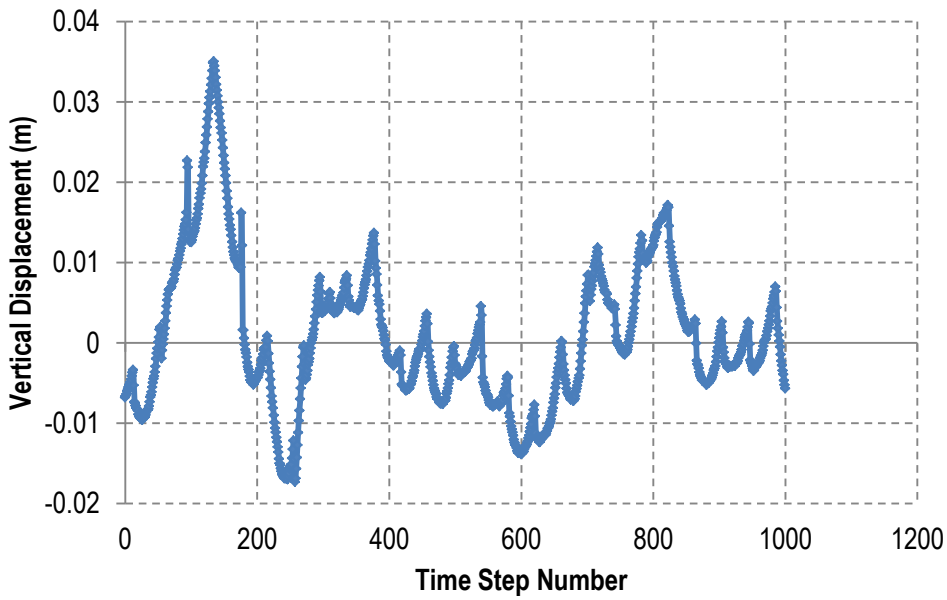

Figure 3.21: Actual road profile plot

Other improvements to the Simulink model include: the incorporation of the EMSA model to the ¼ car model and data exportation to Microsoft Excel for post-processing. The Excel file plots the four states of the system, as well as the sprung mass acceleration. RMS values for the sprung mass acceleration, suspension deflection and tire deflection are calculated. Shown in Table 3.4 is a comparison between a passive system and an active system. The active system provides the desired force to the suspension while the passive system has fixed properties for the suspension. The gains used for the desired force in this case are based upon [2].

Table 3.4 RMS value comparison between passive and active systems

RMS Values	Acceleration of M_s (m/s^2)	Suspension deflection (m)	Tire deflection (m)
Passive	0.129800167	0.002289356	0.000260091
Active	0.081540088	0.002519663	0.000200731

3.2.2.3. Simulation of the F800 Truck Model

The initial simulations for the F800 truck model, using LS-DYNA, were performed in order to obtain the mass, stiffness and damping values for the vehicle body and the wheel/tire assembly.

The sprung mass values were obtained by placing rigid walls under each wheel/tire assembly. Gravity was applied to the model and the resulting forces from the rigid walls were recorded. In order to obtain the steady state results, a forced damping value was applied to the model. Table 3.5 displays the total mass values for each rigid wall. Note that the unit “tonne” is equal to 1,000 kg.

Table 3.5 Total mass values for F800 truck model

Rear Driver [tonne]	Rear Passenger [tonne]	Front Driver [tonne]	Front Passenger [tonne]	Total Mass [tonne]	Actual Total Mass [tonne]	Mass % Difference
2.435	2.368	1.598	1.618	8.019	8.142	1.504

The tire stiffness values were obtained by first removing every component/part of the F800 truck except for the tires, wheel hubs and the rigid walls. A vertical displacement (prescribed motion) was applied to each wheel hub and the resulting reaction force was recorded by the rigid walls. The tires were modeled using air-bag models and are all identical. Figure 3.22 is a plot of the reaction force for the rigid wall vs. the prescribed motion of the wheel hub. The results show that the stiffness for each tire is piecewise linear. The slope of the line shown in Figure 3.22 is the stiffness value for the tire. Since the line is piecewise linear, the tires effectively have multiple stiffness values depending upon the range of deformation. Based on [2], [3] and results obtained from the Matlab-Simulink model, it is assumed that the maximum deformation of the truck tires will not exceed 15 mm. Shown in Figure 3.23 is a plot of the reaction force vs. displacement for the range of interest (0-15mm). It is shown from the regression line in Figure 3.23 that the stiffness for the tires is approximately 6657.3 (kN/m).

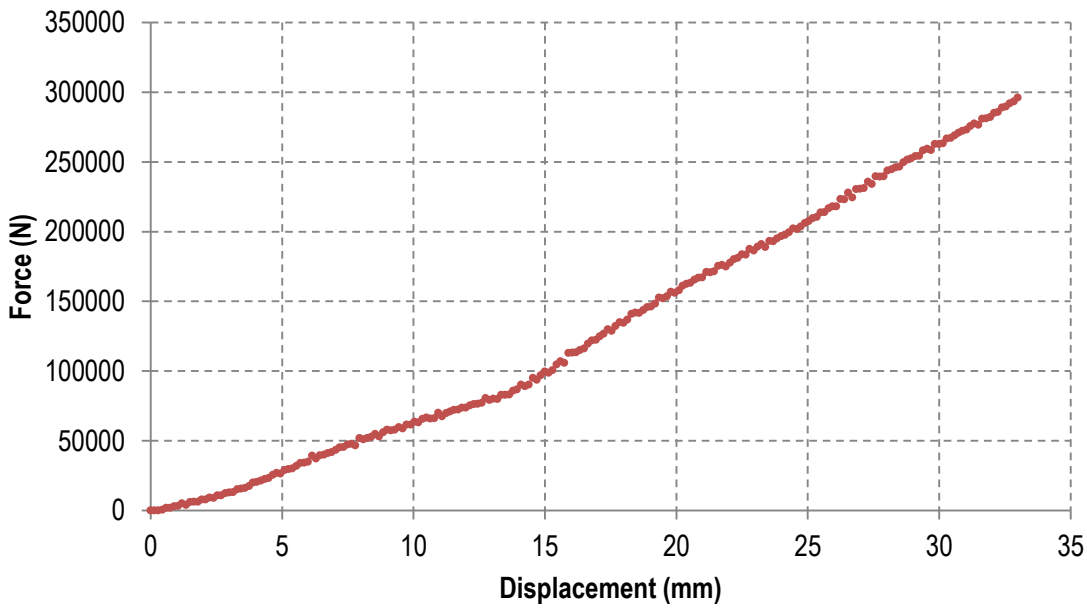

Figure 3.22: Plot of reaction force vs. the prescribed motion

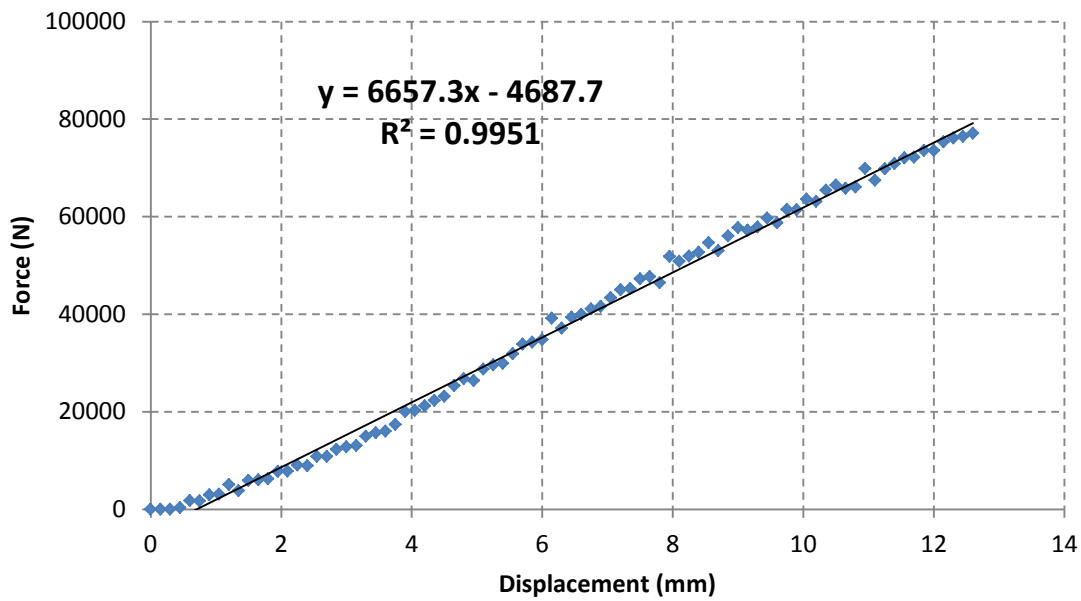

Figure 3.23: Plot of force vs. displacement, for displacements less than 15 mm

The stiffness and damping values for the suspension of the F800 truck have yet to be obtained. Once these are obtained, the gains for the controller can be found. Once the gains are found, the controller can be evaluated in Matlab-Simulink, and further modification may be made in order to find the most suitable values for the gains. A sub-routine in LS-DYNA will then be created to mimic the operation of the controllable EMSA. Simulations will be performed to compare the performance of the EMSA suspension system with the passive suspension system.

3.2.2.4. References

1) Gupta, A.; Jendrzejczyk, J. A.; Mulcahy, T. M.; Hull, J. R.; "Design of Electromagnetic Shock Absorbers", International Journal of Mechanics and Materials in Design, Vol. 3, No. 3, 2007, pp. 285-291.
2) Gao, H.; Lam, J.; Wang, C.; "Multi-objective Control of Vehicle Active Suspension Systems Via Load-dependent Controllers," Journal of Sound and Vibration, Vol. 290, 2006, pp. 654-675.
3) Du, H.; Sze, K.Y.; Lam, J.; "Semi-active H[infinity] control of vehicle suspension with magneto-rheological dampers", Journal of Sound and Vibration, Vol. 283, No. 3-5, 2005, pp. 981-996.

3.3. A Coupling of CFD and CSM Codes for Scour Shape Prediction

3.3.1. Introduction

As detailed in Section 4 of the TRACC Y5Q3 Progress Report, TRACC CFD researchers have been investigating approaches to simulate the formation of scour holes and have been enhancing the

simulation models. A current area being addressed is the unreasonably steep slopes of the scour walls that are produced by the STAR-CCM+ CFD program when a sand slide model is not included.

A very simple sand slide model that does not include soil mechanics models is descriped in the TRACC Y5Q3 report. A second approach to accounting for the effects of sand slides during scour hole formation in non-cohesive sediments is to model the soil mechanics using the structural mechanics software LS-DYNA to compute sand slides. In this approach the CFD simulation calculates soil erosion around the pier while the CSM simulation calculates the slope stability and final slope shape after the material undergoes a sand slide.

3.3.2. Scour Slope Stability Based on Soil Mechanics

In the CFD simulations based on the described approach most of the soil material is eroded in the close proximity to the pier. The deformations tend to be localized and lead to a very steep slope in the scour hole. Comparison to the limited experimental results indicates that this is not the case. Depending on the size of the particles in the river bed, the entrained sand would either be transported away from the scour hole or would be deposited at the bottom of it. Additionally localized erosion of the bed material would cause slope instability and the material would slide creating slopes with the base angle close to the angle of repose for the sand.

In the approach presented here the second phenomenon (sand slide) is addressed through the coupling of the STAR-CCM+ computational fluid dynamics solver with the LS-DYNA multiphysics solver. The soil is treated as a deformable body subject to gravitational forces in the Multi-Material Arbitrary Lagrangian Eulerian (MM-ALE) approach.

Material MAT_005 (Soil and Crushable Foam) was used to model the soil. Volumetric compaction is determined by a tabulated curve of pressure versus volumetric strain defined from a hydrostatic compression test. A pressure-dependent flow rule governs the deviatoric behavior of the model:

$$\phi_s = \frac{1}{2} s_{ij} s_{ij} - (a_0 + a_1 p + a_2 p^2) \tag{3.14}$$

Where:a_0, a_1, a_2 are user-defined constants obtained from triaxial compression test. An example of such failure surface definition is shown in Figure 3.24.

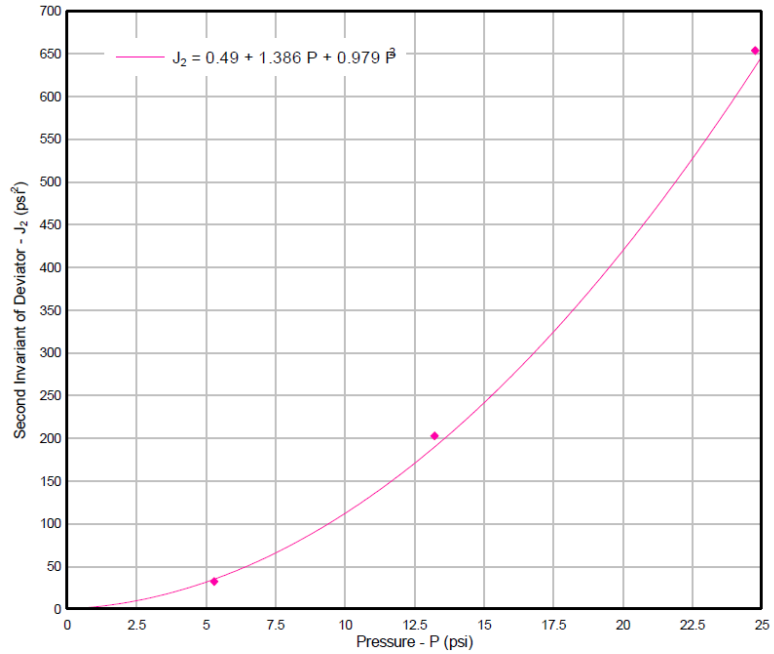

Figure 3.24 Strength envelope in terms of yield surface- second invariant of deviatoric stress and pressure

The shear failure of the soil is occurring when the ϕ_S defined in Equation (3.14) becomes zero. It means that the stress state defined by the second stress invariant is located on the yield surface. This material definition has a simple implication stating that if the confining pressure of the material is very low, accordingly low shear stress would cause the material to fail. In the case of scour slope stability lack of confinement of the sand is causing fluid-like flow of material.

3.3.3. Procedure Flowchart

The procedure consists of the following steps:

1. Run the analysis in STAR-CCM+ up to the point where the slope angle exceeds significantly the natural angle of repose of the sand. (This is the state where deviatoric shear stress in the soil can cause the slope to slide.)
2. Extract the shape of the scour hole in the NASTRAN file format.
3. Import the NASTRAN file to LS-PrePost – a pre and post processor for LS-DYNA.
4. Build a shell container with the shape of the scour for soil volume initialization in the LS-DYNA simulation.
5. Analyze the slope stability problem using LS-DYNA MM-ALE capabilities.
6. Export final shape of the scour to the NASTRAN file that can be imported back to STAR-CCM+.

3.3.4. Simplifying Assumptions

The procedure of this coupling has several simplifications:

1. The shear stresses on the bed surface resulting from the water flow are not transferred in the coupling process – only the geometry is transferred. Due to this assumption the surface shear stress is not contributing to the further slope slide.
2. If the LS-DYNA simulation is executed too early in the scouring process the gravitational forces may have small effect on the soil behavior. That may require long computations for achieving the equilibrium position.
3. State of stress in the soil from LS-DYNA is not transferred back to STAR-CCM+. Gravitational compaction will be occurring each time the transfer between STAR-CCM+ and LS-DYNA is executed.

For these reasons it is not recommended to perform multiple transfers between the two codes. Limiting the transfers to one or two would reduce the errors generated in the coupling process.

3.3.5. Example of Use of the Procedure

Geometry of scour hole with noticeable steep walls was obtained from STAR-CCM+ simulation. Its initial shape is shown in Figure 3.25.

Figure 3.25 Initial scour shape based on STAR-CCM+ calculation

Subsequently the geometry was used to build a volume for soil material initialization in LS-DYNA. Only a portion of the domain around the pier was modeled to save the computational cost. The modeled domain had approximate dimensions of 300 mm x 300 mm x 750 mm for width, height and length respectively. The base size of the background element was ~2.5 mm which resulted in ~3,450,000 uniform hexahedral elements and about 10 elements through the width of the initial scour hole localized deformation. This is a rather large number of elements and should be sufficient to capture the deformation precisely. Figure 3.26 shows the Finite Element model of the scour hole. Only soil and the air are modeled. The water was not included in this model although in the future it can also be represented in the model.

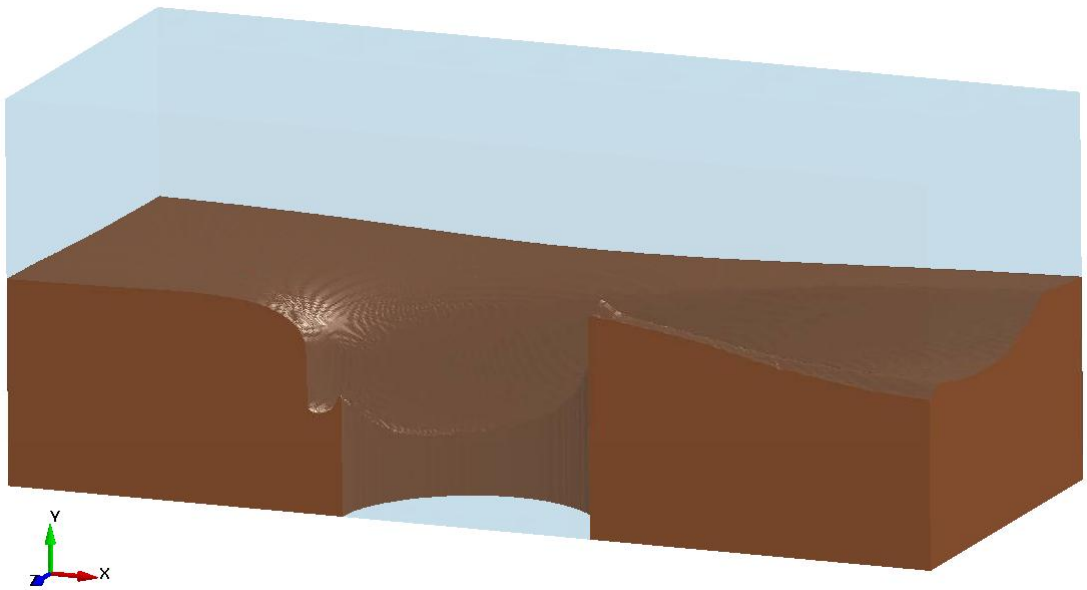

Figure 3.26 Finite Element model of the scour hole – initial state

The LS-DYNA simulation was performed on the TRACC high performance cluster using 8 compute nodes (64 cores). It took approximately 12 hours to get to the state where no further movement of the soil was registered. The final shape of the scour hole is shown in Figure 3.27.

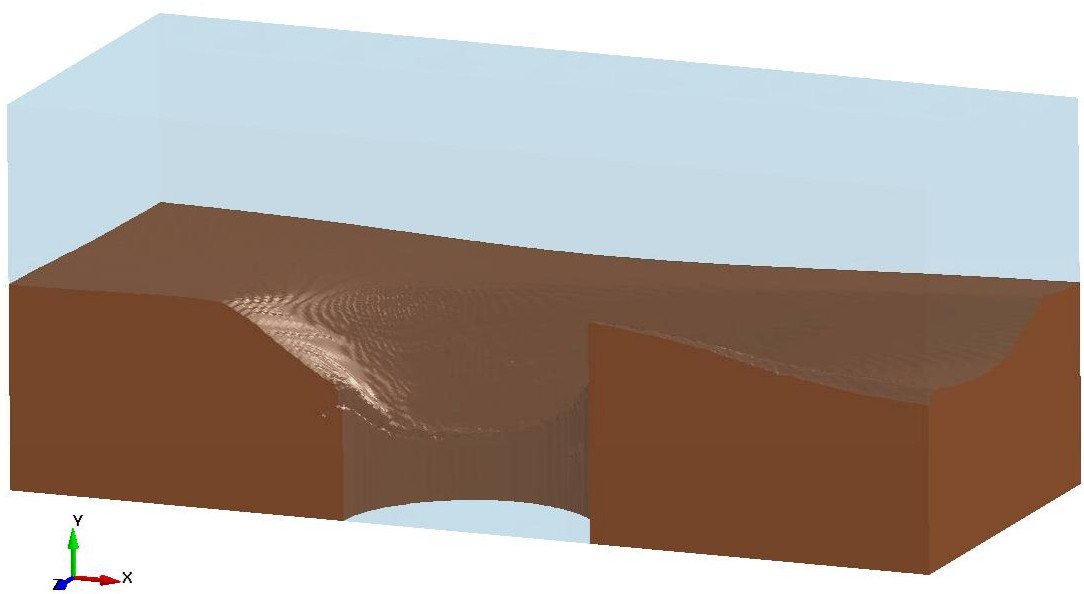

Figure 3.27 Finite Element model of the scour hole – final state

Figure 3.28 shows side by side comparison of the initial and final shape of the scour hole in the LS-DYNA simulation.

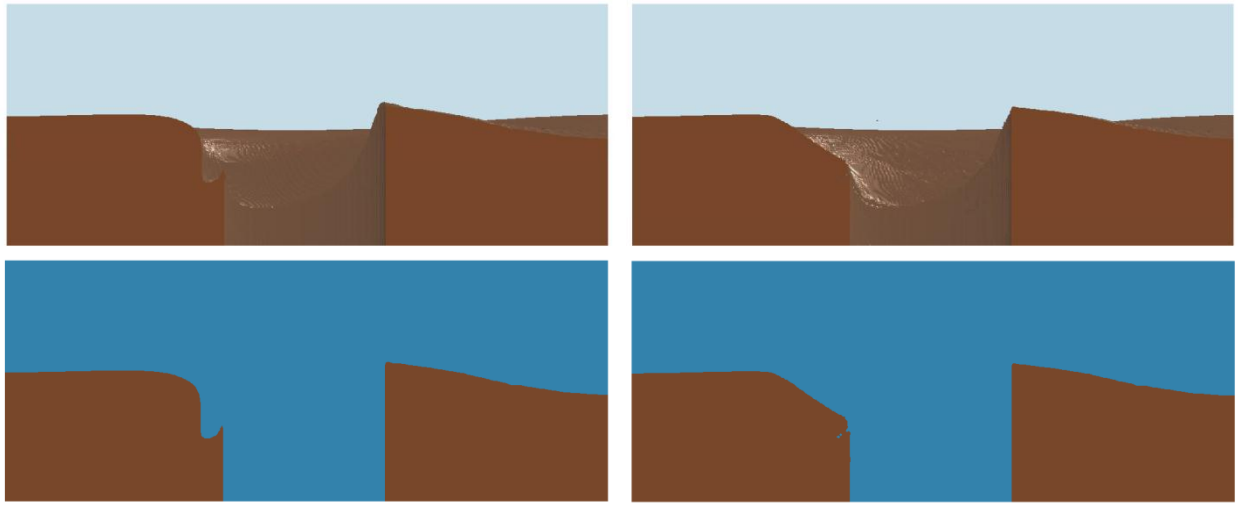

Figure 3.28 Comparison of the initial and the final shape of the scour hole

Energy Systems Division
Argonne National Laboratory
9700 South Cass Avenue, Bldg. 362
Argonne, IL 60439-4815

www.anl.gov

Argonne National Laboratory is a U.S. Department of Energy
laboratory managed by UChicago Argonne, LLC